NARSIS

New Approach to Reactor Safety ImprovementS

WP2: Fragility assessment of main NPPs critical elements

Del2.6 – Methodology to derive vector-based fragility functions I: theoretical aspects

THE FRAMEWORK PROGRAMME FOR RESEARCH AND INNOVATION HORIZON 2020

This project has received funding from the Euratom research and training programme 2014-2018 under Grant Agreement No. 755439.

European Commission

Project Acronym:	NARSIS
Project Title:	New Approach to Reactor Safety Improvements
Deliverable:	Del2.6 – Methodology to derive vector-based fragility functions I: theoretical aspects
Month due:	18 **Month delivered:** 18
Leading Partner:	Bureau de Recherches Géologiques et Minières (BRGM)
Version:	V1

Authors:

- BRGM: Pierre Gehl, Jérémy Rohmer
- EDF: Irmela Zentner
- NCBJ Karol Kowal, Sławomir Potempski
- CEA Cyril Feau
- IRSN Marine Marcilhac-Fradin, Yves Guigueno
- Framatome GmbH Manuel Pellissetti
- KIT James Daniell

Deliverable Review:

- **Reviewer:** Luciano Burgazzi, ENEA **Date:** February 26, 2019

Dissemination Level		
PU	Public	**X**
PP	Restricted to other programme participants (including the Commission Services)	
RE	Restricted to a group specified by the consortium (including the Commission Services)	
CO	Confidential, only for members of the consortium (including the Commission Services)	

Table of contents

List of Figures

List of Tables

List of Abbreviations

AIC	Akaike Information Criterion
BBN	Bayesian Belief Network
CDFM	Conservative Deterministic Failure Margin
DS	Damage State
EDP	Engineering Demand Parameter
GLM	Generalized Linear Model
GMPE	Ground-Motion Prediction Equation
HCLPF	High-Confidence Low Probability of Failure
IM	Intensity Measure
MLE	Maximum Likelihood Estimation
NLTHA	Non-Linear Time History Analysis
NPP	Nuclear Power Plant
PGA	Peak Ground Acceleration
PSA	Probabilistic Safety Assessment
PWR	Pressurized water reactor
RC	Reinforced Concrete
SA	Spectral Acceleration
SSC	Structure, System or Component

1 Executive Summary

This report presents the outcomes of the preliminary work carried out in Task 2.3 (*"Development of methods to derive vector-valued fragility functions in a multi-hazard approach"*) of the NARSIS H2020 project. It presents the methodological basis for the derivation of vector-valued fragility functions, either in the case of multiple intensity measures describing a given hazard loading or in the case of intensity measures related to different hazard events. The procedures and methods detailed in the present report are meant to be applied to the subsequent fragility analysis of critical structures, systems and components, which will take place in the second phase of Task 2.3.

Section 3 of the report consists in a literature review of current approaches for deriving fragility functions for structures, systems and components. An emphasis is put on the treatment of uncertainties and their propagation up to the representation of the fragility functions.

Section 4 of the report is devoted to the case of seismic fragility functions, where the benefits of using vector-based IMs (or "vector-IMs") are discussed from the point-of-view of the reduction of aleatory uncertainty (i.e., record-to-record variability). Two simplified case studies are detailed as examples, i.e. the seismic fragility of a PWR main steam line and the seismic fragility of a fuel assembly grid. For both these applications, the uncertainties induced by scalar-IM fragility curves or vector-IM fragility functions are compared and discussed. Globally, a reduction in the dispersion is observed, although some care should be taken when interpreting vector-IM fragility functions that are based on strongly correlated variables (i.e., ground-motion parameters).

Section 5 of the report investigates multi-hazard fragility functions and puts forward a harmonized framework in order to treat various cases of multi- and single-hazard interactions. As a result, it is found that a total of five cases may be able to describe most of the configurations that are encountered, when dealing with external hazard events:

1. Standard single-IM case, with a simple IM-EDP relationship.
2. Vector-IM fragility function, usually with a correlation between the IMs.
3. System fragility function, resulting from the assembly of single component damage events (i.e., combination of failure modes). The correlation between the occurrences of the failure modes, given the IMs, should be taken into account.
4. Multi-hazard fragility function, where a multi-variate distribution function represents the damage probability due to the interaction of co-occurring loadings.
5. Damage-state-dependent fragility functions where a first hazard loading may degrade the resistance of the SSC or alter the conditions for when a subsequent hazard loading is applied (i.e., sequence of events). The hazards may be correlated (i.e., same source event, or one hazard event triggering another) or independent (i.e., occurrence within the same time window).

2 Introduction

As a crucial step of the Probability Safety Assessment (PSA) of a Nuclear Power Plant (NPP), the vulnerability of the structures, systems and components (SSC) must be quantified with respect to a wide range of external loadings induced by natural hazards. To this end, fragility curves, which express the probability of an SSC to reach or exceed a predefined damage state as a function of an intensity measure representing the hazard loading, are common tools developed in the nuclear industry. Their probabilistic nature make them well suited for PSA applications, at the interface between probabilistic hazard assessments and event tree analyses, in order to estimate the occurrence rate of undesirable top events.

Due to the thousands of SSCs that may be comprised within a NPP, most nuclear regulations advocate the application of Safety Factors methods, which consist in multiplying design level values with factors representing uncertainties due to capacity and demand variability. This approach has been used by practitioners since the 1980s, due to its relative ease of implementation when compared to time-consuming numerical simulations. More recently, the Risk Informed approach has assumed a more relevant role in safety analysis as compared to the safety factor model: it focuses on the evaluation of the “probabilistic margin”, defined by the probability that the load exceeds the capacity.

Therefore, one of the objectives of the NARSIS Work Package 2 is to develop refined fragility derivation methods in order to increase the accuracy of the estimation of SSC failure rates, thanks to current advances in quantitative hazard modelling and computational capacities. Such fragility models are expected to provide the following features:

- Use of multiple intensity measures expressing a given hazard loading, in order to improve its characterization and reduce its inherent randomness: this is mostly the case for seismic loadings, where the temporal and frequency contents of a ground motion record are only imperfectly represented by a single intensity measure.
- Integration of multi-hazard interactions and cumulated effects (succession of events, ageing mechanisms, fatigue, etc.) within a harmonized multi-hazard framework: functionality-based damage states, which account for various and potentially concurring failures modes within a single SSC, will be used, in order to create harmonized and ready-to-use fragility functions for the subsequent safety analysis of the NPP.

To this end, a statistical tool of choice will be vector-based fragility functions, which have the ability to represent probabilities of damage as a function of multiple intensity measures. Moreover, the correlation between intensity measures, failure modes and engineering demand parameters will be appropriately treated thanks to the application of system reliability methods, such as the matrix-based system reliability method (Kang et al., 2010) or the implementation of Bayesian belief networks (BBNs) to describe the chain of damage events (Gehl & D’Ayala, 2016).

Therefore, the aim of this report is to present the methodological basis for the derivation of vector-valued fragility functions, either in the case of multiple intensity measures describing a given hazard loading or in the case of intensity measures related to different hazard events. The effects of integrating multiple intensity measures will be evaluated and discussed for several simple applications, before deriving proper fragility models in the later phase of Task 2.3 (i.e., deliverable report D2.7).

First, a literature review of current approaches for deriving fragility functions for SSCs is performed (Section 3), starting with the initial framework by Kennedy et al. (1980) and analyzing the respective merits of statistical regression methods for the derivation of fragility parameters. Then, Section 4 is mostly focused on the case of seismic fragility functions, where the benefits of using vector-based IMs (or “vector-IMs”) are discussed from the point-of-view of the reduction of aleatory uncertainty (i.e., record-to-record variability): numerical simulations on two applications are exploited in order to derive seismic vector-based fragility functions and to demonstrate the proposed approach. Finally, the case of multi-hazard fragility functions is

investigated in Section 5, where a harmonized framework is put forward in order to treat various cases of multi- and single-hazard interactions.

3 State-of-the-Art Fragility Analysis of SSCs in NPPs

This section provides an overview of current approaches for the derivation of fragility functions for SSCs in the nuclear industry. The review applies mostly to the case of seismic hazard, which has been the object of the most comprehensive studies in the past. Fragility analyses with respect to other natural hazards are discussed in Section 5.

3.1 Theoretical framework

Fragility functions express the probability of reaching or exceeding a damage state DS given the level of seismic loading, represented by an intensity measure IM = *im*. Thus, they are written in the form of conditional probabilities. The damage state is defined by the engineering demand parameter (EDP) exceeding a given threshold: the EDP represent the physical demand that is subjected to the SSC, until its capacity is reached. Depending on the type of SSC and the type of damage mechanism investigated, EDPs may be represented by a wide range of physical variables, such as the maximum deformation during the loading, the stress level reached by a structural element, or the ductility ratio.

Due to the statistical distribution of IMs and EDPs in practical applications, fragility curves are usually represented as a cumulative lognormal distribution (Ellingwood, 1990), as follows:

$$P_f(im) = P(ds \geq DS | IM = im) = \Phi\left(\frac{\ln im - \ln \alpha}{\beta}\right) \quad (1)$$

where α represents the median and β the standard deviation, i.e. the fragility parameters.

Kennedy et al. (1980) and Kennedy & Ravindra (1984) have proposed a formal framework for the treatment of uncertainties related to nuclear applications. The standard dispersion β may be decomposed into:

- a term β_R representing aleatory randomness (e.g., the record-to-record variability);
- a term β_U representing epistemic uncertainty (e.g. modelling or parameter uncertainties due to lack of knowledge).

Therefore, they have proposed the following mathematical expression, which allows the definition of a family of fragility functions for various confidence levels *Q*:

$$P_f(im) = \Phi\left(\frac{\ln im - \ln \alpha + \beta_U \Phi^{-1}(Q)}{\beta_R}\right) \quad (2)$$

Thus, the epistemic uncertainty on the estimation of the median α, due to lack of knowledge for instance, is represented by the standard deviation β_U. As a result, the value Q = 0.5 yields the median fragility function, which may be flanked by a set of fragility functions representing confidence intervals (e.g., Q = 0.05 and 0.95 for the 5%-95% confidence interval). On the other hand, the aleatory uncertainty, represented by β_R, directly acts on the general shape of the curve (i.e., the "slope").

Within this framework, it is also possible to aggregate both types of uncertainty into a composite fragility function with a larger dispersion:

$$P_f(im) = \Phi\left(\frac{\ln im - \ln \alpha}{\sqrt{\beta_U^2 + \beta_R^2}}\right) \quad (3)$$

Such an expression represents the mean fragility function, for which the total dispersion is obtained through a quadratic combination of β_U and β_R:

$$\beta_C = \sqrt{\beta_U^2 + \beta_R^2} \quad (4)$$

The graphical constructions related to these mean and median fragility functions are illustrated in Fig. 1.

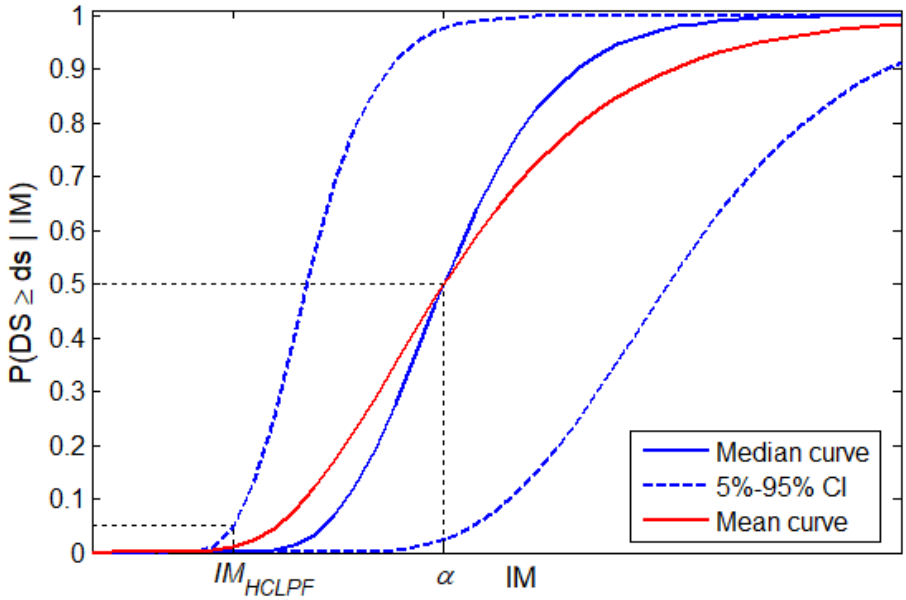

Fig. 1: Representation of the mean and median fragility functions, along with their 5%-95% confidence interval.

Finally, this uncertainty decomposition enables the computation of the so-called HCLPF (High Confidence Probability of Failure) capacity, which corresponds to the intensity measure leading to a failure probability of 5% on the 95% confidence curve. From Equation 2, it may be expressed as follows:

$$IM_{HCLPF} = \alpha \cdot \exp[-1.645(\beta_U + \beta_R)] \quad (5)$$

The HCLPF capacity has a practical use in the seismic margin assessment framework, where the capacities of all components may be assembled in order to quantify the capacity of the NPP. Such an approach leads to the identification of "weak links" and to the estimation of the plant's capacity to withstand beyond-design earthquakes (i.e., margin with respect to the safe shutdown earthquake).

3.2 The safety factor method

Due to the large number of SSCs within a NPP, a simplified approach for the estimation of seismic fragility parameters has been developed for nuclear application (EPRI, 1994). This method assumes a given seismic design level IM_s (i.e. the intensity measure corresponding to the design event). The median fragility parameter α is evaluated from the design level, through a safety factor F that represents the seismic margin adopted during the design stage:

$$\alpha = IM_S \cdot F \quad (6)$$

In the case of structures, the safety factor F is decomposed into three categories (EPRI, 2009):

$$F^{(struct)} = F_S \cdot F_\mu \cdot F_{SR} \quad (7)$$

where F_s is the strength factor, F_μ is the energy dissipation factor and F_{SR} is the structural response factor, which is further decomposed as follows (see definition of factors in Table 1):

$$F_{SR} = F_{SA} \cdot F_{GMI} \cdot F_\delta \cdot F_M \cdot F_{MC} \cdot F_{EC} \cdot F_{SSI} \quad (8)$$

In the case of an equipment within a structure, the safety factor *F* takes the following form (EPRI, 2009):

$$F^{(equip)} = F_S \cdot F_\mu \cdot F_{SR} \cdot F_{ER} \quad (9)$$

where the strength factor F_s and the energy dissipation factor F_μ now refer to the behaviour of the equipment; F_{SR} is the structural response factor, and F_{ER} is the equipment response factor (relative to the structure).

Table 1: Definition of the structural response factors used in the safety factor method

Safety Factor	Definition
F_{SA}	Spectral shape factor
F_{GMI}	Factor related to the spatial incoherency of ground motion
F_δ	Damping factor
F_M	Modelling factor
F_{MC}	Factor related to the structural mode combination rules
F_{EC}	Factor related to the combination of horizontal earthquake components
F_{SSI}	Soil-structure-interaction factor

These factors are evaluated through various means, such as seismic design calculations, engineering judgement, plant walkdown past earthquake experience, or qualification through testing or numerical analysis (static or dynamic). Depending on the estimation method used and on the type of safety factor, various levels of standard deviations $\beta_{U,i}$ and $\beta_{R,i}$ are proposed for each of the safety factor F_i. Thanks to the lognormal assumption, a quadratic combination is used to assemble the global uncertainty terms β_U and β_R from the list of safety factors. The following equation is an example of the computation of β_U for a structure:

$$\beta_U = \sqrt{\beta_{U,S}^2 + \beta_{U,\mu}^2 + \beta_{U,SA}^2 + \beta_{U,GMI}^2 + \beta_{U,\delta}^2 + \beta_{U,M}^2 + \beta_{U,MC}^2 + \beta_{U,EC}^2 + \beta_{U,SSI}^2} \quad (10)$$

The EPRI (2003) and EPRI (1994) guidelines contain recommendations and standard values for some of the safety factors and their associated uncertainty terms.

3.3 Regression models from numerical simulations

For specific types of critical SSCs, more in-depth analyses than the safety factor method are required. Numerical analyses of structural models of SSCs are an efficient way to generate a cloud of data points representing IMs and EDPs, for instance through non-linear time-history analyses (NLTHAs). Two main types of statistical regression are then used for the derivation of the fragility parameters (see Fig. 2).

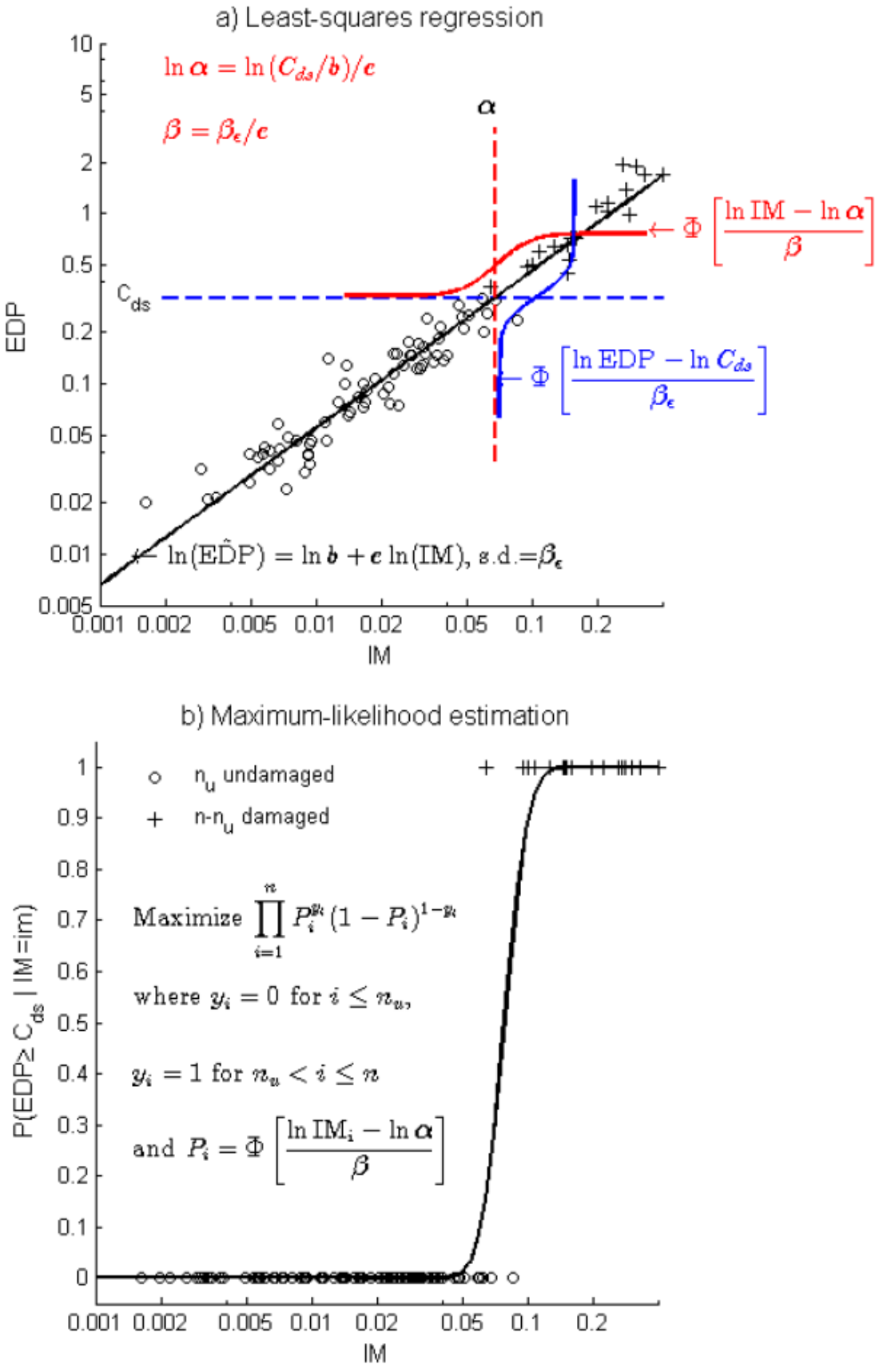

Fig. 2: Schematic representation of the derivation of fragility curves using: (a) least-squares regression and (b) maximum-likelihood estimation – Taken from Gehl et al. (2015).

3.3.1 Regression on the IM-EDP cloud

First, Cornell et al. (2002) have proposed to perform a least-squares regression on the IM-EDP dataset, i.e. the so-called "regression on a cloud". It is based on the lognormal assumption, where the following functional form is regressed from the data points:

$$\ln \widehat{edp} = a + b \ln im + \varepsilon \quad (11)$$

The error term ε is also assumed to follow a normal distribution, of mean zero and standard deviation σ.

Therefore, by identifying the terms of the fragility function in Equation 1, the fragility parameters α and β are expressed as follows:

$$\begin{cases} \alpha = \exp\left(\frac{\ln EDP_{th} - a}{b}\right) \\ \beta = \frac{\sigma}{b} \end{cases} \quad (12)$$

where EDP_{th} corresponds to the response of the SSC (e.g., deformation, drift, stress values) that is considered to be threshold of the studied damage state.

Due the simplicity of this model, the least-squares regression tends to yield stable estimates, even with a reduced number of data points (Gehl et al., 2015). Therefore, it is possible to estimate fragility parameters even when very few simulation outcomes exceed the damage threshold. However, the extrapolation of the regression beyond the IM interval defined by the data points should be avoided. Moreover, as seen in Equation 12, the standard deviation β is independent from the damage state threshold, which means that all curves would present the same "slope" (in the lognormal space) if different grades of damage states were to be studied from the same dataset: this constraining assumption does not necessarily comply with the variability in the response of the studied SSC when higher loading levels are applied (i.e., increased dispersion.

3.3.2 Regression using a binomial distribution

Alternatively, another approach consists in applying a Generalized Linear Model (GLM) regression or a maximum likelihood estimation (MLE) to a set of binary damage variables *Y*: all points that exceed the damage state threshold take the value $y_i = 1$, and 0 otherwise. This statistical approach has been introduced by Shinozuka et al. (2000).

As a result, due to the independent sampling of successes and failures given IM, the *Y* variables follow a binomial or Bernoulli distribution. Thus, the likelihood function of the fragility parameters α and β, given *N* data points, takes the following form:

$$L(\alpha, \beta) = \prod_{i=1}^{N} \left[P_f(im_i, \alpha, \beta)\right]^{y_i} \left[1 - P_f(im_i, \alpha, \beta)\right]^{1-y_i} \quad (13)$$

Then, a maximization of *L* through a search algorithm leads to the best estimates of the fragility parameters α and β.

In the GLM framework, a linear combination of the input (i.e. ln *im*) is estimated from the distribution of the *Y* variables:

$$f\left[P_f(im)\right] = c_1 + c_2 \ln im \quad (14)$$

If the link function $f = \Phi^{-1}$ (i.e. *probit* model), the fragility function can be written as:

$$P_f(im) = \Phi(c_1 + c_2 \ln im) \quad (15)$$

Then, by identification with Equation 1, the fragility parameters are expressed as follows:

$$\begin{cases} \alpha = \exp\left(-\frac{c_1}{c_2}\right) \\ \beta = \frac{1}{c_2} \end{cases} \quad (16)$$

The MLE approach provides the same numerical outcomes as the GLM regression when the *probit* (i.e., inverse of normal cumulative distribution) is used as the link function *f*. Other link functions have been proposed, such as the logistic or Poisson model; however, the *probit* model presents the benefit of generating a lognormal cumulative distribution function, which stays within the original fragility framework.

The use of a binomial distribution does not require exact values of EDP, as long as the simulation outcomes that exceed the damage threshold are identified. Therefore, this approach may be more suited in case the studied SSC is experiencing strong non-linear behaviour (e.g., near the collapse state), which cannot be accurately modelled by the simulation tools. For a given damage state threshold, a clear separation between intact and damaged states is made, which leads to the estimation of a damage-state-specific standard deviation β. Moreover, this approach does not rely on a linear relation between the logarithms of IM and EDP, which is often not justified when plotting the data points. However, a stable estimation of the fragility parameters requires a larger amount of data points and, especially, an appropriate balance between SSC responses that are below and over the damage state threshold.

A comparison between the least-squares regression and the maximum likelihood estimation has been performed by Zentner et al. (2017), using the outcomes of NLTHA on the numerical model of a shear wall building (i.e., SMART2013 benchmark): the authors point out the stability issue in the estimation of the fragility parameters, when data points are not well balanced around the damage state threshold. However, they conclude that the MLE method offers more possibilities to consider various types of IM, since this approach is not constrained by the expression of a log-linear relation between IM and EDP. Another comparison between the least-squares regression and the GLM regression has been conducted by Rossetto et al. (2016), through a static capacity spectrum analysis of RC buildings: a noteworthy conclusion is the ability of the GLM regression to account for the heteroscedastic nature of the structural response (i.e., increasing dispersion from light to severe damage state), when considering more than one damage states.

Finally, a few observations regarding the two main regression methods are worth mentioning:

- Both methods assume a lognormal cumulative distribution for the fragility functions: this hypothesis is convenient since it ensures compatibly with current hazard and risk models; however other functional forms would deserve to be explored (Sudret et al., 2017), especially around the tails of the distribution. When applying the MLE approach or the GLM regression, it is however possible to assume other functional forms, if needed (e.g., (e.g., the extreme value distribution). Classical information criteria such as BIC allow for choosing the best among the available models (Zentner et al., 2017).
- While using numerical simulations to derive fragility functions, it remains possible to distinguish between aleatory and epistemic uncertainty terms, thus ensuring the compatibility with the aforementioned theoretical framework. For instance, in the case of seismic hazard, the record-to-record variability may represent the aleatory randomness; and a confidence interval around the fragility function can be estimated by considering the variability of modelling parameters or the dispersion in the statistical estimates (i.e., epistemic uncertainty). For instance, this decomposition has been demonstrated by Zentner (2010), who has applied the MLE approach to the seismic fragility analysis of a reactor coolant system.

3.4 Other methods

Other fragility derivation methods may be used, such as the Incremental Dynamic Analysis or the Bayesian updating framework, which are summarised below.

3.4.1 Incremental Dynamic Analysis

The Incremental Dynamic Analysis (IDA) is based on numerical simulations where a set of accelerograms is scaled to have same intensity level (Vamvatsikos & Cornell, 2002). Given a set of accelerograms, *N* nonlinear time history analyses are performed for each intensity level. The set of *N* accelerograms is scaled to increasing intensity levels, until failure is reached. Uncertainties of the structure are considered by using one set of *N* uncertain parameters, to be used for all intensity levels. Using this method, each accelerogram has a single capacity value associated with onset of collapse.

The distribution of capacity and thus the fragility can be derived from this sample. One can for example, estimate the median and the standard deviation of the lognormal distribution. The sample of structural capacities can also be used to estimate an empirical probability function by kernel density smoothing. The fragility curve is then obtained by integration as the cumulative density function.

Sometimes, the probability of collapse at a given intensity level is evaluated as the fraction of records for which collapse occurs at a level lower than the threshold. This is however not recommended from a statistical point of view since the sample size used with IDA (at most two dozens) is not sufficient to estimate failure probabilities.

The maximum likelihood estimator is not applicable to IDA since the results at different increments are not independent (i.e., same scaled accelerograms, same set of sampled random parameters). Vamvatsikos & Cornell (2002) propose to use 10-20 time histories when performing IDA, and in ATC-58 (2012) a number of 20 time histories is recommended. Clearly, this number strongly depends on the output that has to be computed. If only the median capacity is requested, then a few time histories are sufficient to obtain good estimates of that quantity. The estimation of dispersion (in terms of standard deviation) requires a greater sample size. For comparison, EPRI recommends to use 30 time histories and transient analysis for the evaluation of probabilistic floor spectra (median and log std). Interestingly, ATC-58 (2012) recommends the use of IDA only for the evaluation of the median capacity while tabulated values should be used for the β-parameter of the lognormal fragility curve. This is motivated by the small number of time analyses and by the fact that epistemic uncertainty is generally not fully accounted for in the numerical analysis. Eventually, Vamvatsikos & Cornell (2002) recommend to perform 10 analysis per record, which is a compromise between computational cost and accuracy.

3.4.2 Bayesian updating

The Bayesian updating framework allows for combining the results of numerical simulations and damage data to construct fragility curves (Wang et al., 2018). Expert judgement or the results of numerical simulations provide a prior estimation of the seismic capacity of the equipment. The estimation of the uncertainty related to the equipment capacity can be taken from the literature. Damage data, collected from the in-situ observation and the database of the seismic qualification utility group (SQUG), are then used to construct the likelihood function for the Bayesian updating.

The damage data has been collected for equipment located at different floor levels. The location of the equipment has an impact on the load and thus the possible failure. This is why a transformation method has to be applied to transform the load in the SQUG database to the load experienced by the studied equipment.

Given a lognormal fragility model, the likelihood function reads:

$$L(A_m|im,\chi) = \prod_{i=1}^{N}\left[P_f(\alpha_i)\right]^{y_i}\left[1-P_f(\alpha_i)\right]^{1-y_i} \quad (17)$$

The observed data is the sample of (im_i, y_i), i = 1,...N, pairs, where y has the same meaning as in Equation 13. Failure and survival occur with probability $P_f(\alpha_i)$ and $\left(1-P_f(\alpha_i)\right)$, respectively. The updated fragility parameters are determined from the respective posterior distributions:

$$f_{post}(A_m) = \propto L(A_m|,im,\chi)f(A_m) \quad (18)$$

In the framework of the double lognormal fragility model used in nuclear engineering, $f(A_m)$ is a lognormal distribution with median equal to the median capacity of the structure and log standard-deviation β_U expressing the epistemic uncertainty related to the evaluation of the latter. If the posterior distribution of A_m is close to lognormal, then the updated median capacity and log standard-deviation can be directly plugged into the double lognormal fragility model of Equation 2. Otherwise the family of fragility curves has to be evaluated numerically.

Another approach consists in updating both the median capacity and the parameters characterizing the random uncertainty β_R:

$$f_{post}(A_m,\beta_R) = \propto L(A_m,\beta_R|,im,\chi)f(A_m)f(\beta_R) \quad (19)$$

This allows for a "further degree of freedom" in the updating procedure.

3.5 Summary of statistical methods

Following the above descriptions, a short analysis of the main features and limits of the statistical methods for the derivation of fragility functions is presented in Table 2.

Table 2: Comparative analysis of the characteristics of various statistical methods for the derivation of fragility functions

Approach	Main feature	Added value	Main Limits	Example of application
Least squares Regression	Regression of a log-linear IM-EDP relationship.	- Simple and intuitive approach; - Stable fragility estimates may be obtained with a few data points;	- Constrained by the functional form of the IM-EDP relationship; - Constant standard-deviation over the IM range	- seismic fragility of an RC structure (Seyedi et al., 2010);
MLE-based regression / GLM regression	Maximisation of the likelihood function, built from damage and no-damage events.	- Applicable to empirical fragility assessment (if only damage data are available); - Ability to treat complete damage/collapse cases (where EDP values are usually inaccurate); - Compatible with multivariate regression;	- Loss of information (i.e., the true values of the EDP are not used); - More data points are required to achieve stable fragility estimates;	- seismic fragility of a masonry structure (Gehl et al., 2013); - empirical tsunami fragility of buildings (De Risi et al., 2017);

Incremental Dynamic Analysis	Successive scaling of the ground-motion records.	- Accurate estimation of the fragility parameters (i.e., extraction of robust statistical distributions);	- Designed for seismic analysis only; - Loss of the seismic hazard consistency when large scaling factors are used;	- seismic fragility of an NPP RC building (Zentner et al., 2017);
Bayesian updating	Updating of the prior distribution of fragility parameters thanks to observations.	- Compatible with expert-judgment approaches or experimental results;	- Influence of the prior distribution on the final fragility estimates;	- seismic fragility of switchgear cabinets (Wang et al., 2018)

3.6 Discussion on uncertainties

In general, there are two major types of uncertainties: aleatory (i.e. the inherent variability of the measurable physical quantities, such as design parameters or mechanical properties) and epistemic ones (coming from lack of complete knowledge about the modelled phenomena, incomplete data or modelling assumptions). While the first type is irreducible, the second one (including finite sample uncertainty, in-situ uncertainty and loading protocol uncertainty) may be reduced over time by some additional measures and testing. Currently, fragility functions are developed mainly using experimental, numerical and observational data, and thus are generally expected to represent the aleatory uncertainties in the process being modelled. However, the epistemic uncertainties should be also addressed in fragility functions developed for use in seismic performance assessment. The sources of epistemic uncertainties in fragility functions, their consideration, combination, and propagation has been presented and thoroughly discussed in several publications (e.g. Bradley, 2010; Bradley, 2013; Roueche et al., 2018). This subsection synthesizes the information contained in these and other relevant papers.

By definition, fragility functions provide the probability of incurring, or exceeding, a specific discrete damage state as a function of some EDP. Thus, the uncertainties in the determination of the distribution parameters of the fragility functions lead to the uncertainty in the damage states' probabilities. In order to assess the latter, it is useful to describe the probability of being in a specific damage state ($DS = ds_i$) for a given level of the ground motion intensity measure ($IM = im$) by the following formula:

$$P(ds_i|im) = \int_{EDP} P(ds_i|edp) f(edp|im) \mathrm{d}edp \cong \sum_j w_j \, P\left(ds_i|edp_j\right) f\left(edp_j|im\right) \quad (20)$$

where $P(ds_i|edp)$ is the probability of being in $DS = ds_i$ given $EDP = edp$; $f(edp|im)$ is the probability density function for the seismic response of $EDP = edp$, conditioned on $IM = im$; and w_j is the numerical integration weight (Kythe & Schaferhotter, 2000).

Assuming both $P(ds_i|edp)$ and $f(edp|im)$ as uncertain variables, one can determine the uncertainty in $P(ds_i|edp)$ either by simulations or analytical methods. For example, the expectation and variance of the discrete form derived above can be described as follows:

$$E[P(ds_i|im)] \cong \sum_j w_j \, \mu_{X_f} \mu_{Y_j} \quad (21)$$

$$Var[P(ds_i|im)] \cong \sum_j \sum_k \{w_j w_k (\sigma_{X_j X_k} \sigma_{Y_j Y_k} + \mu_{X_f} \mu_{X_k} \sigma_{Y_j Y_k} + \mu_{Y_f} \mu_{Y_k} \sigma_{X_j X_k})\} \quad (22)$$

where $X_j = P\left(ds_i|edp_j\right)$; $Y_j = f\left(edp_j|im\right)$; μ_{X_j} is the expectation of X_j; $\sigma_{X_j X_k}$ is the covariance of X_j and X_k. The uncertainty in $f\left(edp_j|im\right)$ have been investigated by Dolsek (2009). The expectation and variance of $P\left(ds_i|edp_j\right)$ for a given $EDP = edp$ can be described as follows:

$$E[P(ds_i|edp)] = E[F_i] - E[F_{i+1}] \quad (23)$$

$$Var[P(ds_i|edp)] = Var[F_i] + Var[F_{i+1}] - 2Cov[F_i, F_{i+1}] \quad (24)$$

where the fragility function $F_i = F(ds_i|edp)$. Thus, determination of the epistemic uncertainty in damage states requires both knowledge of the mean and variance in the damage state fragility curves, as well as the covariance between the different damage state fragility curves.

The primary cause of epistemic uncertainties in fragility functions is that of limited high quality data. Firstly, this means that the parameters defining the fragility function (i.e., the median and dispersion) are determined based on a finite sample of data representing the population and are estimated based on statistics. This uncertainty is commonly referred to as *finite sample uncertainty* and it is related to the number of independent data points used to determine the fragility functions. In order to characterize the uncertainty in the distribution parameters based on *finite sample uncertainty* either the analytical (e.g. Ang & Tang, 2017) or sampling methods can be applied with the most versatile being bootstrap sampling (Wasserman, 2004). Bootstrap sampling involves sampling with replacement from the finite dataset. For each bootstrap sample the desired statistics (mean and variance) are computed. This process is then repeated *N* times, giving *N* different values of the sample mean and sample variance from which other statistics can be obtained. In the limit as the number of bootstrap samples tends to infinity, the results tend toward those obtained analytically.

Secondly, one aspect of data quality refers to how well the conditions under which the data were obtained simulate the conditions in which the component exists in the reality. This uncertainty is usually referred to as *in-situ uncertainty* and can be caused, among others, by:

- testing a component isolated from its in-situ conditions,
- imperfect simulation of boundary conditions for the in-situ,
- extrapolation to in-situ conditions not fully simulated in the test,
- variability in the in-situ configuration.

Another aspect of data quality is the method in which the seismic demand is imposed on the specimen. Naturally, the employment of a loading history cannot precisely replicate the loading experienced by components in a real building responding to earthquake shaking. This type of uncertainty is referred to as *loading protocol uncertainty*. In assessing loading protocol uncertainty it is beneficial to distinguish between the three common forms of seismic testing: dynamic shake table; quasi-static; and pseudo-dynamic:

- the shake table apparatus can impose severe limitations due to the scale effect since the specimens are tested at reduced size (Abrams, 1996; Leon & Deierlein, 1996);
- the quasi-static testing means that larger specimens are tested and no consideration is given to the strain rate effects (Abrams, 1996);
- pseudo-dynamic testing performed on full scale sub-assemblages in real time offers significant reductions in bias and uncertainty in regard to the scale and strain rate effects but there are also various typical assumptions such as constant axial loads, constant shear-to-moment ratios and boundary conditions (Leon & Deierlein, 1996).

Data obtained from the post-earthquake reconnaissance explicitly considers many of the deficiencies of current laboratory experimental methods identified above. However, the empirical fragility functions are usually developed from damage observations and hazard intensity measurements or estimates for multiple damage sites. The damage observations are typically obtained through field or remote investigations, whereas the intensity measures are often estimated from numerical models conditioned to the specific hazard events. Thus, the degree of uncertainty in empirical fragility functions can vary significantly from one post-hazard damage assessment to another, depending upon the attention to detail in the preparation and conducting of the assessment, the quality and quantity of the data available, and the choice of methods in obtaining the fragility functions from the empirical damage data (Roueche et al., 2018). Moreover, development of empirical fragility functions relies upon the appropriate selection of numerical models of the IM distribution throughout the affected region. For

earthquakes, the IM distribution is often estimated using various ground motion prediction equations (GMPEs), which predict the IM based upon explanatory parameters such as the earthquake source and distance from it, wave propagation path, and local site conditions (Stewart et al., 2015). It should be noted here that, until 2018, as much as 450 different GMPEs for peak ground acceleration have been developed (Douglas, 2018). In all of these models, uncertainty is present in the model parameters, which are often based upon judgment and general observations rather than direct measurements. Thus, for a given hazard event, there often exists an ensemble of IM distributions that are plausible, which contributes to the uncertainty in empirical fragility functions.

Another source of uncertainty in empirical fragility functions is the dependency between the data collected that, among others, may come from the following reasons:

- similarity in the ground motion experienced by two different components;
- observations of the same component during multiple earthquakes;
- similarity in in-situ conditions of components (i.e., installed by the same contractor).

There are several methods that can be employed to account for such dependencies in the observed data that have been described in (Straub & Der Kiureghian, 2008).

Moreover, if experimental or observational data are used to develop fragility functions, then correlations within the different parameters of the fragility functions could occur due to similarities in the loading protocol, as well as uncertainties in the material properties and geometry of the components. Determination of the correlation of epistemic uncertainties can be either accomplished using simulation, expert judgement, or both.

In conclusion, the discussion about the uncertainties associated with the performance-based earthquake engineering framework should always cover both aspects, i.e. the site-specific input ground-motion history data and the system-specific models of the expected seismic response. The analytical framework of the ground-motions analysis accounts for the fact that:

(i) seismic hazard is posed by numerous seismic sources;
(ii) there is uncertainty in the likelihood of a specific source rupture in a given time interval;
(iii) there is uncertainty in the ground-motion characteristics at a site from a specific source rupture.

Naturally, there is also uncertainty in the seismic capacity/resistance of the system considered, as represented by the seismic response analysis model employed. This uncertainty results from the inability of an idealized numerical seismic response model to predict the actual response of an engineered system to ground motions. It is useful to divide them for the following categories:

(i) uncertainties in the measurement of physical quantities;
(ii) uncertainty in the correlation between measurable physical quantities and constitutive model parameters;
(iii) uncertainty in selecting an appropriate constitutive model;
(iv) uncertainty in the overall idealized model methodology due to the fact that the numerical model domain always represents a gross simplification of reality (e.g. one-dimensional/two-dimensional analyses, neglect of the interaction of specific components, assumed boundary conditions and formulation of damping).

There were some previous studies, which have concluded that ground-motion uncertainty is generally significantly larger than numerical seismic response modelling uncertainty and thus the last one may be neglected. However, such theses were based on the typically biased results, because the ground-motion uncertainty was often overestimated while the numerical modelling uncertainty was generally significantly underestimated when the higher-level modelling uncertainties were neglected (Bradley, 2013). It shows that the appropriate understanding of uncertainties associated with this type of analyses is especially important due to the fact, that the results are not only to provide another quantitative outcome, but to support the decision-making process under uncertain conditions.

4 Case of Seismic Hazard: Vector-Valued IMs for Uncertainty Reduction

This section is devoted to the case of seismic fragility analysis, where methods using vector-valued IMs are demonstrated, with the objective of reducing the associated uncertainty (i.e., record-to-record variability).

4.1 Criteria for the selection of scalar IMs

One of the main issues of current fragility functions pertains to the representation of a complex ground-motion time history by a scalar IM: such an assumption potentially ignores essential measures related to the severity of the external loading, such as the frequency or energy content, the duration of the strong motion, the number of loading cycles, etc.

As a result, with the same IM level (e.g. *PGA*), different ground motions records have to ability to induce different levels of structural response (i.e., the so-called record-to-record variability). The selection of an appropriate scalar IM as an input to a fragility function should therefore help conveying the most information possible from the ground-motion time histories that are used in the numerical simulations. For instance, Luco & Cornell (2007) have started to propose some criteria for an adequate IM selection:

- The *efficiency* of an IM represents the ability of an IM to induce a low dispersion in the distribution of the structural response (i.e., fragility curve with a steep "slope"). The efficiency is measured by evaluating the standard deviation σ of the error term ε in the log-linear relation between IM and EDP (i.e., Equation 11): the lower the standard deviation, the more efficient the IM.
- The *sufficiency* of an IM represents the ability of an IM to "carry" the characteristics of the earthquake that has generated the ground motion: a sufficient IM should render the distribution of EDP conditionally independent, given the IM, from the magnitude and the distance of the related earthquake events. Using Equation 11 again, the sufficiency of an IM can be checked qualitatively by plotting the residuals of the regression with respect to the magnitude or the distance. In other words, an IM is assumed to be sufficient is the following equality is verified (Luco & Cornell, 2007):

$$P\left(EDP\middle|\ddot{x}_g\right) = P\left(EDP\middle|IM\left(\ddot{x}_g\right)\right) \tag{25}$$

where the term x_g represents the whole range of acceleration time-histories that can occur at the considered site. This definition refers, of course, to an ideal case. Therefore Jayaler et al. (2011) introduce the concept of relative sufficiency, which measures the additional quantity of information provided by an IM_2 with respect to a reference IM_1:

$$I(EDP|IM_2|IM_1) = \int log_2 \frac{P\left(EDP\middle|IM_2\left(\ddot{x}_g\right)\right)}{P\left(EDP\middle|IM_1\left(\ddot{x}_g\right)\right)} \cdot p\left(\ddot{x}_g\right) \cdot \mathrm{d}\ddot{x}_g \tag{26}$$

If IM_2 is more sufficient than IM_1, then the relative sufficiency index I will be positive, and vice versa. The use of the base 2 logarithm enables an interpretation of the results in terms of bits of information. Finally, the integration over all possible ground motions at the site requires accurate knowledge of the hazard level and of the relative contributions of each seismic zone at the given site.

Moreover, Padgett et al. (2008) have proposed additional metrics in order to assess an IM, such as:

- *Practicality*: this metric reflects the strength of the link between IM and EDP. A practical IM will generate a large slope (i.e., coefficient *b* in Equation 11) in the log-linear relation between IM and EDP.
- *Proficiency*: this metric combines practicality and efficiency, since it is evaluated as the ratio b/σ in Equation 11. A high ratio (i.e., high practicality, high efficiency) means a proficient IM.
- *Computability* (or *Hazard compatibility* – cf. Hariri-Ardebili & Saouma, 2016): this essential criterion checks whether the selected IM may be computed accurately with current GMPEs, in order to ensure the link between the fragility function and the probabilistic seismic hazard curve.

Computability is a qualitative concept; however, the following grades may be proposed:

1. IM associated with many well-constrained GMPEs thereby providing an estimate of the epistemic uncertainty;
2. IM associated with few well-constrained GMPEs and it is hence difficult to judge the epistemic uncertainty;
3. IM associated with no reliable GMPEs.

This classification is used to assign the considered IMs to one of the three categories (see Table 3), based on the existing GMPEs in the literature (Douglas, 2012 ; Douglas, 2018).

Table 3: Qualitative assessment of the computability of some IMs. Appendix A summarizes the definition of the ground-motion parameters that are considered as potential IMs.

Computability grade	IM
1	PGA, PGV, AI, SA(T), RSD75, RSD95
2	PGD, ASI, SI, NED, JMA, CAV, NCy
3	ARMS, A95, SL75, SL95, SMA, SMV, DCy

Finally, most of the aforementioned metrics are specific to the SSC considered (i.e., strong link with the vibration mode of the component) and to the studied site (i.e., location and characteristics of the seismic sources generating the ground-motion time histories). The derivation of fragility functions should therefore be associated with an *ad hoc* study of the most relevant IMs, for a given case study.

4.2 Introduction of vector-valued IMs

Experience has shown that finding a scalar IM that fulfils all the aforementioned criteria is usually not feasible. For instance, the sufficiency criterion is especially difficult to be fully satisfied by a single IM, which is why the relative sufficiency measure has been introduced (Jalayer et al., 2011).

Therefore, Baker & Cornell (2005) have introduced an additional IM, epsilon ε (i.e., the deviation between the spectral acceleration of a record and the mean of a ground motion prediction equation at a given period), which is used as a proxy for the spectral shape of the time history, in order to reduce the dispersion in the prediction of the mean annual collapse rate.

Seyedi et al. (2010) have applied the concept of seismic fragility surfaces (e.g., use of two IMs as predictors) to an eight-story regular frame RC structure. Using the outcomes of NLTHAs, the spectral displacements at the periods of the first two vibration modes have been selected as IMs, based on the strength of the correlation between IMs and EDPs. As a result, fragility surfaces have been derived by estimating the fragility parameters for ‘slices’ of the space described by the two IMs (i.e. fitting of a fragility function over a primary IM while keeping the secondary IM constant within a given interval, or ‘slice’).

A similar framework has been exploited by Gehl et al. (2013), who have derived fragility surfaces for a two-story unreinforced masonry building. A Receiver Operating Characteristics (ROC) analysis has been performed in order to test the adequacy of dozens of scalar IMs and vector-valued IMs. Thus, the area under the ROC curve provides a quantitative metric for the objective selection of the IMs. Two cases have been considered, i.e. when the two IMs are almost orthogonal (i.e., IM_1 = PGV and IM_2 = PGA/PGV) and when they are strongly correlated (IM_1 = SA at 0.15s and IM_2 = SA at 0.5s): the correlated case implies a rigorous investigation of the IM_1-IM_2 space that is actually explored by the ground-motion records used in the NLTHAs, in order to avoid any double-counting of the record-to-record variability.

Modica & Stafford (2014) have also searched for the most efficient vector-valued IMs, with respect to a series of European low- and mid-rise reinforced concrete frames. They have found that the most efficient vector corresponds to a combination of SA and a spectral shape parameter (i.e., *Np* – Bojorquez & Iervolino, 2011), when used to predict maximum inter-storey drifts. Since their fragility derivation procedure is based on least-square regressions, Modica & Stafford (2014) have also investigated the effect of introducing heteroskedasticity in the statistical distribution of EDP given IM: this feature potentially has a significant impact on the final shape of the fragility functions, especially at lower IM values (i.e. left tail of the cumulative distribution).

Seismic fragility surfaces have also been applied to other types of structures, such as RC bridges (Li et al., 2014): in that study, the authors select SA at the periods of the first two vibration modes as a vector-valued IM, in order to derive fragility functions for each of the bridge's components. Following the definition of damage states for the bridge system, the component fragility functions are assembled while considering the correlation matrix between component-specific damage events. With the vector-valued IM comprising SA are two different periods, Li et al. (2014) have also accounted for the correlation between the two ground-motion parameters: as a result, the fragility surface for the bridge system is only represented for the IM combinations that are actually realistic, given the seismic hazard characteristics of the studied site.

Within the specific context of the fragility analysis of structures and components in NPPs, Cai et al. (2018a,b) have introduced a simplified approach for the derivation of fragility surfaces. It is not based on time-consuming NLTHAs, since it relies on ground response spectra where different spectral values are sampled in order to model the seismic demand. The fragility parameters are then estimated with the safety factor method, with respect to two IMs. Finally, a weighting scheme is applied in order to combine the respective contribution of the multiple ground-motion parameters, in accordance with the distribution of the related seismic hazard.

Recently, Sainct et al. (*submitted*) have proposed a methodology based on Support Vector Machines (SVMs) coupled with an Active Learning algorithm to derive a proficient IM from a reduced number of numerical calculations. In practice, input excitation is reduced to some relevant IMs and then SVMs are used for a binary classification of the structural responses relative to a limit threshold of exceedance. Since the output is not binary but a real-valued score, a probabilistic interpretation of the output is exploited to estimate very efficiently fragility curves as score functions. Thus, with appropriate kernels, the score function can be viewed as an efficient IM since a perfect classifier would lead to a fragility curve in the form of a unit step function when the problem is linearly separable. In addition, the score function is find to be highly correlated with the EDP (in the logarithmic scale), so it can be considered as a practical IM. This methodology also allows to derive easily fragility curves as functions of classical IMs (e.g PGA).

4.3 Application: Fragility analysis of a PWR main steam line

This section demonstrates the derivation of vector-valued fragility functions, or fragility functions, through NLTHAs of a PWR steam line. Procedures for the selection of input ground-motions records, the selection of IMs and the derivation of the fragility functions are detailed.

4.3.1 Description of the studied model

For demonstration purposes, the coupled model of a supporting structure and a secondary system (Rahni et al., 2017) is considered here, corresponding to the main steam line of a PWR. The model is built and computed with the CAST3M finite-element software. Structural elements, representing the containment building, are modelled with multi-degree-of-freedom stick formulations. The containment building has a double-wall structure, with an inner reinforced prestressed concrete wall and an outer reinforced concrete wall. The inner wall is modelled by means of four sticks with Timoshenko beam elements. The outer wall and internal structures are represented with simply sticks located at the structure's centre of gravity (see Fig. 3).

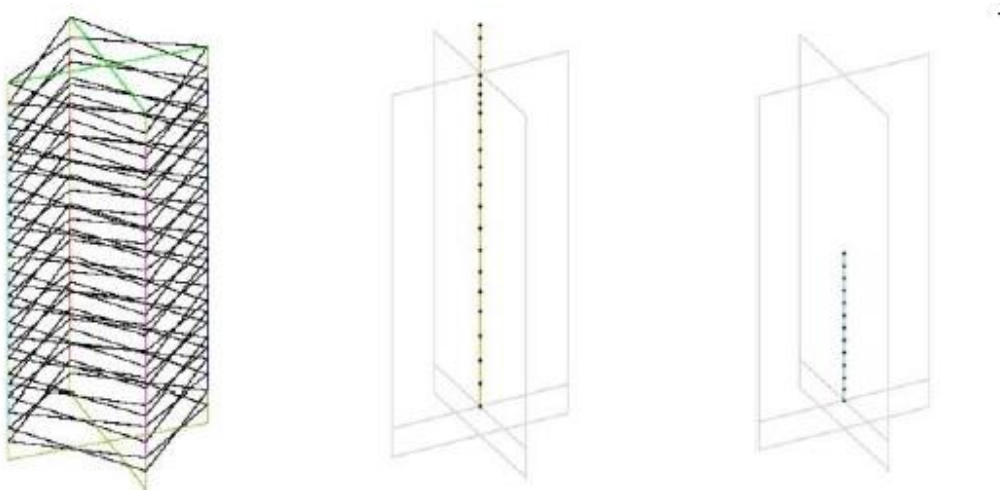

Fig. 3: Stick modelling of the outer wall (left), the inner wall (middle) and the internal structures right) – Taken from Rahni et al. (2017).

The steam line is modelled by means of right pipe, elbow and beam elements, taking in consideration the steel steam line, and several valves, supporting devices and stops at different elevations of the supporting structure (see Fig. 4). The stick models, which have the benefit of enabling fast computations, have been calibrated from detailed finite-element 3D models of the containment building (Rahni et al., 2017).

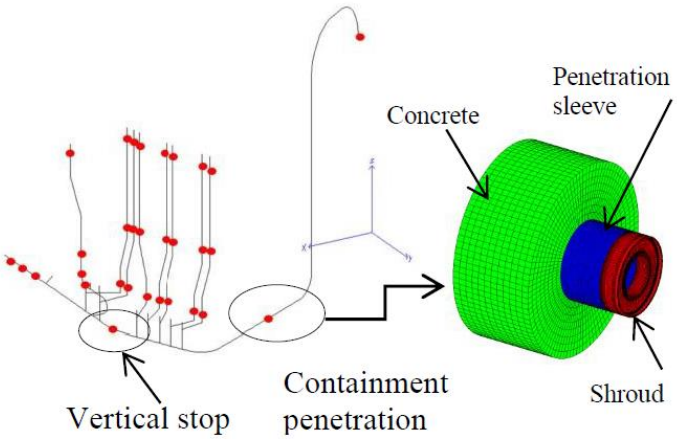

Fig. 4: Steam line beam model and containment penetration model – Taken from Rahni et al. (2017).

Rahni et al. (2017) have proposed several mechanical failure criteria for the verification of the steam pipe line integrity:

- the equivalent stress at any point of the pipe line (conservative assumption);
- the total plastic deformation at the pipe location corresponding to the containment penetration, accounting for the non-linear behaviour of the steel material;
- the effort calculated at the beam model's node corresponding to the vertical stop.

For simplicity purposes, the latter failure criterion is considered here for the fragility analysis (i.e., the exceedance of a given effort value at the point of the steam line corresponding to the vertical stop). Rahni et al. (2017) have also identified this failure mode as the most likely to occur, given the applied seismic loadings.

As a preliminary to the non-linear time-history analyses, a modal analysis of the supporting structure is carried out, in order to identify the main vibration modes (see Table 4).

Table 4: Modal analysis of the model of the containment building.

Mode #	Period [s]	3D Mass participation factor [%]
1	0.38	61
2	0.38	65
3	0.15	35
4	0.14	97
5	0.14	31
6	0.10	2
7	0.09	3
8	0.06	2

Modes #1 and #2 correspond to the excitation of the structure in the *Y*- and *X*-direction, respectively: due the almost symmetrical properties of the building, they are almost identical. Therefore, the fundamental period of the structure is taken as T_1 = 0.38s, while the second one is taken as T_2 = 0.15s (i.e., cluster of modes #3, #4 and #5).

4.3.2 Seismic input for non-linear time-history analyses

As revealed in previous studies, considering multiple ground-motion parameters as vector-valued IMs requires maintaining the consistency of the seismic hazard. Therefore, it is proposed here to apply the conditional spectrum method (Lin et al., 2013) for the selection of the input ground motions. This approach has the benefit of enabling a light scaling of a set of natural records, while saving the consistency of the associated response spectra. Therefore, it is especially suited for the use of spectral values, such as SA at various periods.

The ground-motion selection using conditional spectrum implies the evaluation of the seismic hazard at a given site, along with the identification of reference earthquakes at various return periods: as a result, this approach leads to site-specific fragility functions, which are well suited to the context of NPPs.

The adopted ground-motion selection procedure hinges upon the following steps:

1. ***Selection of the studied site:*** for illustration purposes, the site for the steam line application is chosen arbitrarily in Southern Europe, within a seismically active area.
2. ***Choice of a conditioning period:*** SA at T_1 = 0.38s (fundamental mode of the structure) is selected as the ground-motion parameter upon which the records are conditioned and scaled.

3. ***Definition of seismic hazard levels:*** six hazard levels are arbitrarily defined, and the associated annual probabilities of exceedance are quantified with the OpenQuake engine (www.globalquakemodel.org), using the SHARE seismic source catalogue (Woessner et al., 2013). The GMPE from Boore et al. (2014) is used to generate the ground motions, assuming soil conditions corresponding to $V_{s,30}$ = 800 m/s at the considered site. Data associated with the mean hazard curve are summarized in Table 5.

Table 5: Estimation of the seismic hazard distribution for the studied site.

Scaling level	SA(0.38s) [g]	Annual Probability of Exceedance
#1	0.185	4.87E-2
#2	0.617	4.99E-3
#3	0.836	2.50E-3
#4	1.492	5.00E-4
#5	2.673	5.00E-5
#6	3.882	5.00E-6

4. ***Disaggregation of the seismic sources and identification of the reference earthquakes:*** for the studied site, the OpenQuake engine is used to perform a hazard disaggregation for each scaling level. A reference earthquake scenario may then be characterized through the variables [M_w; R_{jb}; ε] (magnitude, Joyner-Boore distance, epsilon of the ground-motion prediction equation), which are averaged from the disaggregation results (Bazzurro & Cornell, 1999). This disaggregation leads to the definition of a mean reference earthquake (MRE) for each scaling level (see Table 6).

Table 6: Characteristics of the mean reference earthquake (MRE) for each scaling level.

Scaling level	MRE characteristics		
	M_w	R_{jb} [km]	ε
#1	6.22	19.3	1.05
#2	6.55	7.8	1.25
#3	6.65	6.5	1.41
#4	6.80	5.3	1.86
#5	6.96	5.0	2.44
#6	7.57	5.0	2.75

5. ***Construction of the conditional spectra:*** for each scaling level, the conditional mean spectrum is built by applying the GMPE to the identified MRE. For each period T_i, it is defined as follows (Lin et al., 2013):

$$\mu_{ln\,SA(T_i)|\,ln\,SA(T^*)} = \mu_{ln\,SA}(M_w, R_{jb}, T_i) + \rho_{T_i,T^*} \cdot \varepsilon(T^*) \cdot \sigma_{ln\,SA}(M_w, T_i) \quad (27)$$

where $\mu_{\ln SA}(M_w,R_{jb},T_i)$ is the mean output of the GMPE for the MRE considered, ρ_{Ti,T^*} is the correlation coefficient between $SA(T_i)$ and $SA(T^*)$ (Baker & Jayaram, 2008), ε(T*) is the epsilon value at the target period T^* = 0.38s (see Table 6), and $\sigma_{\ln SA}(M_w, T_i)$ is the standard deviation of the logarithm of $SA(T_i)$, as specified by the GMPE.

The associated standard deviation is also evaluated, thanks to the following equation:

$$\sigma_{ln\,SA(T_i)|\,ln\,SA(T^*)} = \sigma_{ln\,SA}(M_w, T_i) \cdot \sqrt{1 - \rho^2_{T_i,T^*}} \quad (28)$$

The conditional mean spectrum and its associated standard deviation are finally assembled in order to construct the conditional spectrum at each scaling level. The conditional mean spectra are represented in Fig. 5, along with the uniform hazard spectra (UHS) that are estimated from the hazard curves at various periods. As stated in Lin et al. (2013), the *SA* value at the conditioning period corresponds to the UHS, which acts as an envelope for the conditional mean spectrum.

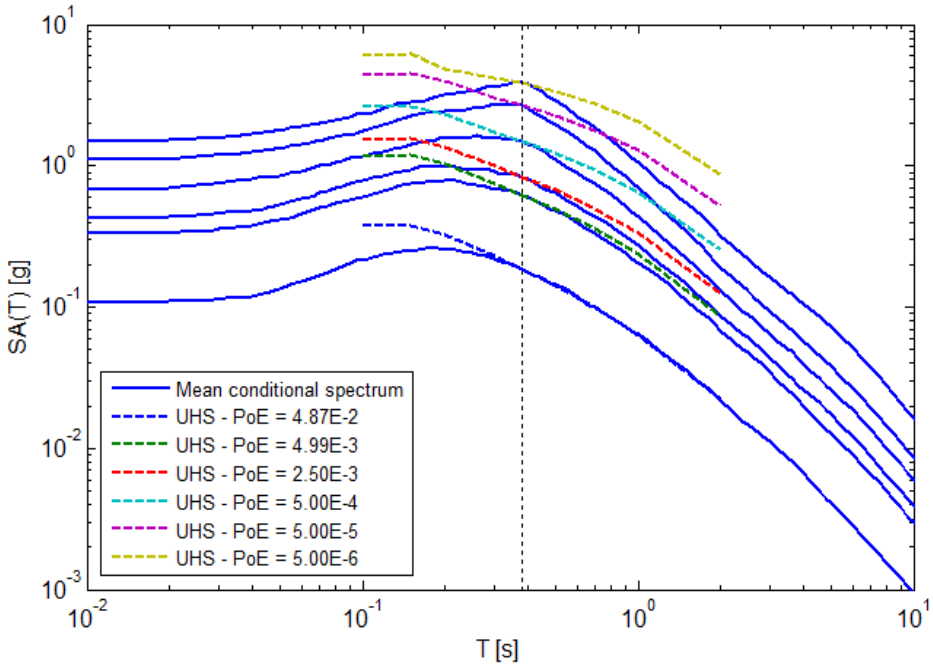

Fig. 5: Conditional mean spectra and uniform hazard spectra for the 6 scaling levels.

6. ***Selection and scaling of the ground-motion records:*** ground-motion records that are compatible with the target conditional response spectrum are selected, using the algorithm by Jayaram et al. (2011) implemented in a Matlab routine (https://web.stanford.edu/~bakerjw/gm_selection.html). The final selection from the PEER database (PEER, 2013) consists of 30 records for each of the 6 scaling levels (i.e., 180 ground-motion records in total), as illustrated in Fig. 6.

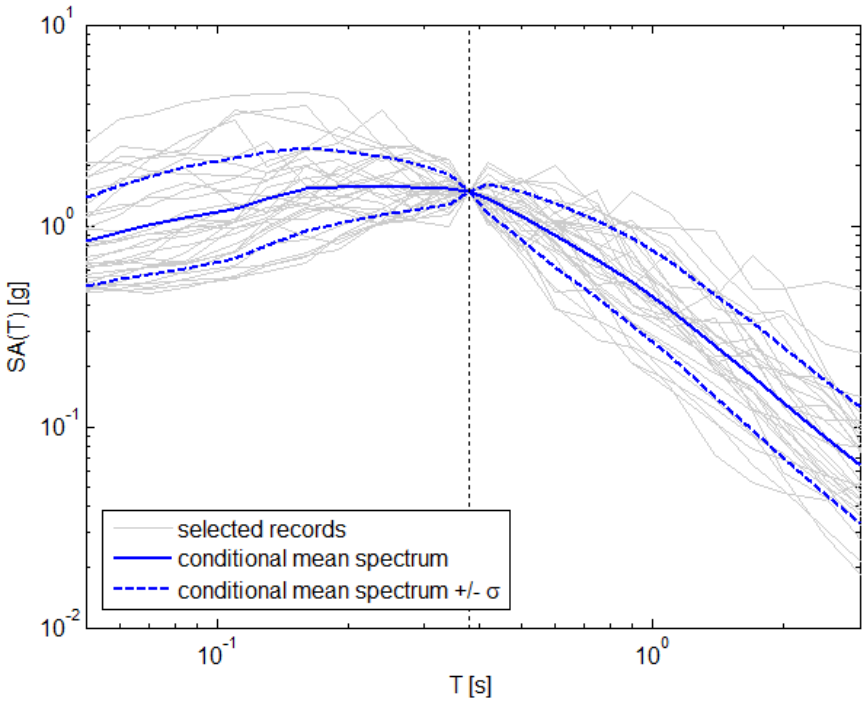

Fig. 6: Conditional spectrum for scaling level #4 and corresponding set of 30 selected ground-motion records.

4.3.3 Derivation of scalar-IM fragility functions

The 180 ground-motion records are applied to the base of the 3D model of the PWR building, in the form of a 3-component loading. In order to integrate the epistemic uncertainties due to the identification of some mechanical and geometrical parameters, ten variables are sampled within a Latin Hypercube Sampling design (see Table 7), following the values provided by Rahni et al. (2017).

Table 7: Range of variation of the ten uncertain parameters considered, based on Rahni et al. (2017). A uniform distribution is assumed.

Variable	Definition	Uniform distribution interval
E_{IC}	Young's Modulus – Inner containment	[27700 – 45556] MPa
ξ_{RPC}	Damping ratio – reinforced prestressed concrete	[4 – 6] %
ξ_{RC}	Damping ratio – reinforced concrete	[6 – 8] %
e_1	Pipe thickness – Segment #1	[29.8 – 38.3] mm
e_2	Pipe thickness – Segment #2	[33.3 – 42.8] mm
e_3	Pipe thickness – Segment #3	[34.1 – 43.9] mm
e_4	Pipe thickness – Segment #4	[33.3 – 42.8] mm
e_5	Pipe thickness – Segment #5	[53.4 – 68.6] mm
e_6	Pipe thickness – Segment #6	[34.1 – 43.9] mm
ξ_{SL}	Damping ratio – steam line	[1 – 4] %

In total, 360 models of the PWR structure are built in the CAST3M environment, so that each ground-motion record may be applied to two different models, with the objective of generating enough data points.

The criterion for the occurrence of the damage state considered (i.e., failure at the vertical stop) is arbitrarily set at EDP_{th} = 400 kN for the maximum transient stress at the vertical stop: this choice is made in order to obtain a relatively good balance between data points

corresponding to intact or damaged states, for demonstration purposes. As an example, some simulation outcomes are presented in Fig. 7, with respect to PGA and SA(0.5s).

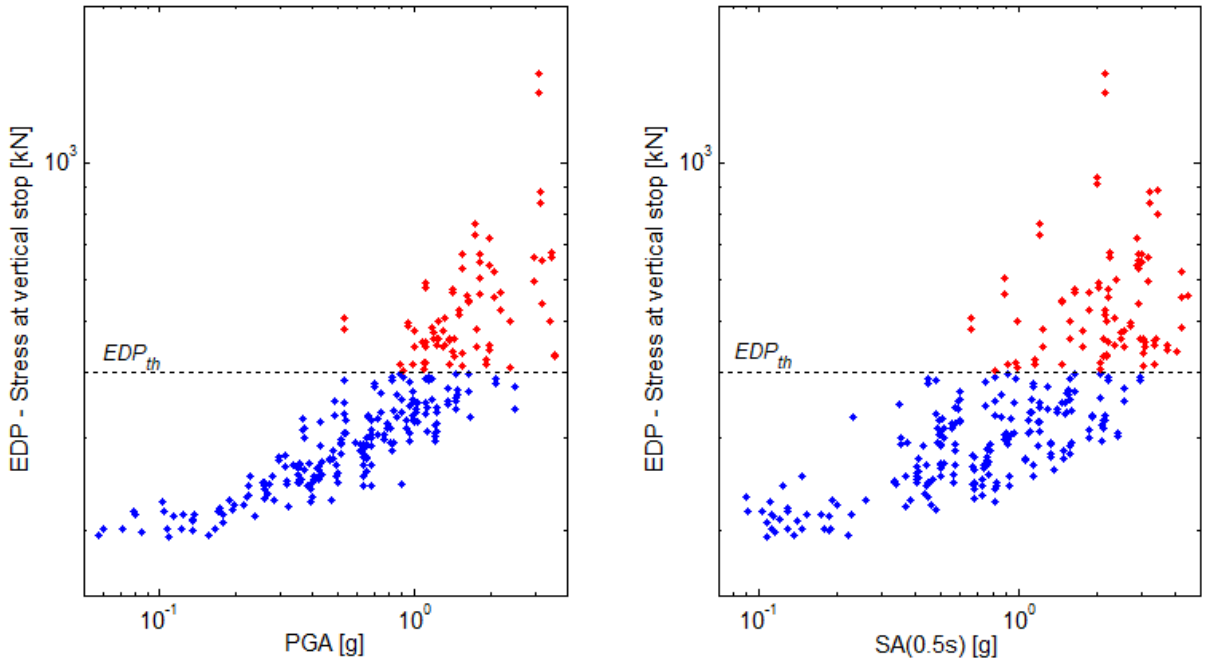

Fig. 7: IM-EDP data points, with respect to PGA (left) and SA(0.5s) (right).

From Fig. 7, it may be observed that a linear fit between the logarithms of IM and EDP is not justified for this specific case study: while Rahni et al; (2017) have applied a Box-Cox transformation to linearize the data, it is proposed here to use the MLE approach, which only requires a separation between the intact and damaged states (i.e., respectively blue and red points in Fig. 7).

To this end, a large number of ground-motion parameters is evaluated as potential IMs (see definitions in Appendix A):

- Spectral acceleration at various periods: *SA*(*T*)
- Peak parameters: *PGA*, *PGV*, *PGD*
- Arias Intensity parameters: *AI*, *A95*, *SL75 (95)*
- Spectral intensities: *SI*, *ASI*
- Duration parameters: *RSD75 (95)*
- Cyclic parameters: *NCy*, *DCy*
- Energy-related parameters: *NED*
- Parameters related to time-integrated acceleration: *CAV*, *ARMS*

It is then proposed to use three performance metrics in order to estimate the adequacy of these potential IMs:

1. **Standard-deviation *β* of the fragility curve:** although the MLE approach is used here, the estimated dispersion parameter *β* may be interpreted as the quantity described in Equation 12, which actually corresponds to the aforementioned *proficiency* measure.
2. **Akaike Information Criterion (AIC):** this criterion quantitatively assesses the goodness-of-fit of a given model. The AIC accounts for the number of parameters used in a model through the variable *k*, in order to penalize the over-parametrization of some models. In the case of scalar-IM fragility curves, *k* = 2 (i.e., parameters *α* and *β*). The AIC is then expressed as follows:

$$AIC = 2k - 2\ln L \qquad (29)$$

where *L* is the likelihood function of the fragility model, which is computed as a product of the 360 conditional probabilities corresponding to the 360 simulation outputs. Therefore, a small AIC value implies a great model fit.

3. **Area under the ROC curve (AUC):** the ROC curve is a possible representation of a ROC analysis, where the ability of a given model to be both specific and sensitive is evaluated by plotting the true positive rate versus the false positive rate. This approach has been applied by Gehl et al. (2013) to the evaluation of fragility curves (i.e. ability of the model to accurately predict the damage state or not, given an IM taken as a predictor). Therefore, the AUC provides a quantification of how well the fragility model works as a classifier: a large AUC value (i.e., area close to 1) implies a model that works significantly better than a random classifier (i.e., the 1:1 diagonal).

These three criteria are first estimated for *SA* at various periods, ranging from 0.05s to 2s (see Fig. 8). The curves reveal an optimum at T = 0.29s, whatever the metric considered. Local optima are also found at periods equal to 0.14s and 0.50s. The three identified periods are close to the periods that corresponding to the first two vibration modes (i.e., T_1 = 0.34s and T_2 = 0.15s). However, they are not exactly identical, and these differences may be explained by two factors, i.e. *(i)* the combination of superior modes that may be excited by some ground motions and *(ii)* the lengthening of the fundamental period due to the loss of elasticity of the structural components.

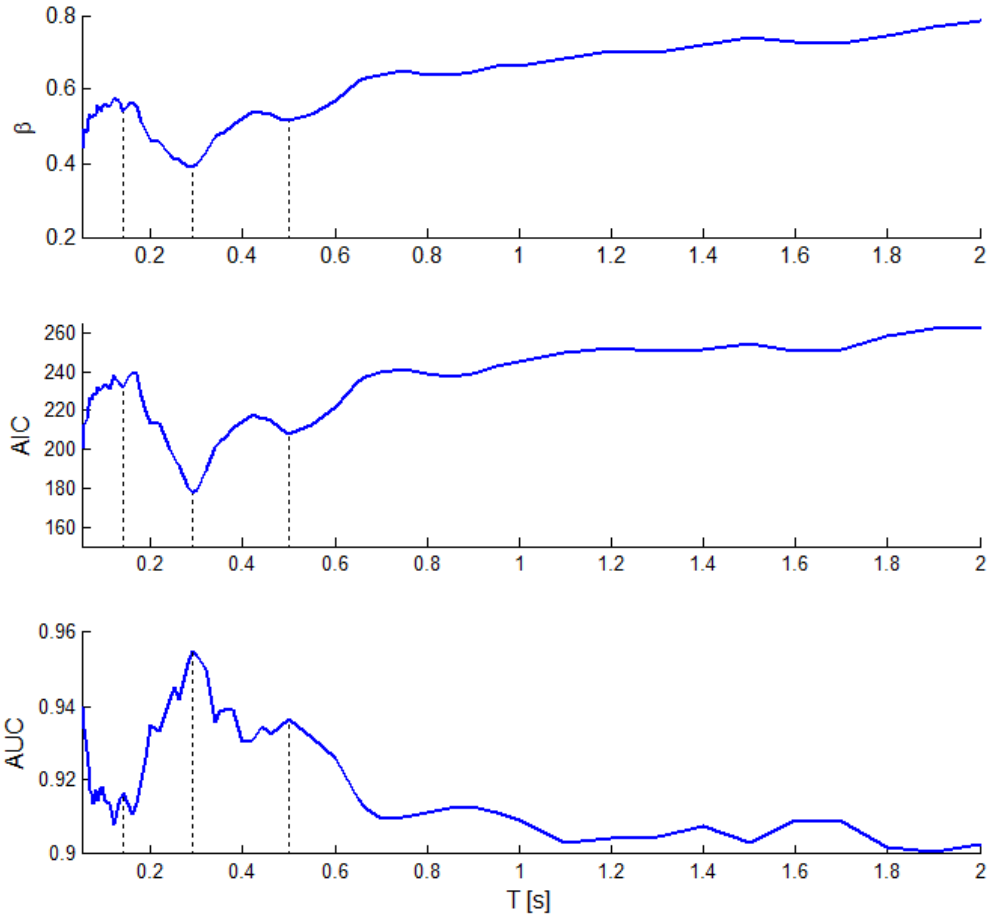

Fig. 8: Evolution of the three performance metrics considered, with SA at different periods.

As a result, *SA* at the three identified periods (0.14s, 0.29s and 0.50s) are considered as potential IMs; and their performance is compared to the one of other ground-motion parameters (see Table 8).

Table 8: Estimated values of the three performance metrics, for different potential IMs. The gray cells indicate the five best performing IMs, for each metric.

IM	β	AIC	AUC
SA(0.14s)	0.5415	229.91	0.9166
SA(0.29s)	0.3898	175.82	0.9547
SA(0.50s)	0.5144	206.12	0.9363
PGA	0.4403	198.45	0.9399
PGV	0.4928	205.73	0.9381
PGD	1.2622	308.93	0.8469
AI	0.7674	182.13	0.9485
A95	0.4041	192.88	0.9389
SL75	0.9471	206.91	0.9325
SL95	0.7681	176.59	0.9508
SI	0.5293	213.94	0.9347
ASI	0.3775	176.23	0.9519
RSD75	-	-	-
RSD95	-	-	-
NCy	-	-	-
DCy	0.8123	191.58	0.9412
NED	1.4284	259.27	0.8968
CAV	0.6012	247.15	0.8951
ARMS	0.5728	240.45	0.9073

It is found that the parameters *SA*(0.29s) and *ASI* are the most consistent, since they show a satisfying performance across the three metrics. Other well performing parameters are *PGA*, *PGV*, *AI*, *A95*, *SL95* and *Dcy*. However, it should be noted that *DCy*, *SL95* and *A95* may not be easily computed from current GMPEs (see Table 3). The metrics cannot be evaluated for some parameters (*RSD75*, *RSD95*, *NCy*) because the fragility estimation has not converged due the poor IM-EDP correlation: these parameters may still be used as secondary IMs when deriving fragility surfaces, if the right IM combination is found.

Finally, as an example, fragility curves with respect to four IMs (*SA* at 0.29s, *ASI*, *PGA*, *AI*) are displayed in Fig. 9, along with the confidence intervals on the statistical estimation. The confidence bounds are estimated with a bootstrap technique, where data points are successively taken out from the IM-EDP dataset. These intervals may then be interpreted as the epistemic uncertainty that is due to the statistical method for the estimation of the fragility parameters (i.e., this uncertainty is expected to decrease as the number of NLTHAs is increased).

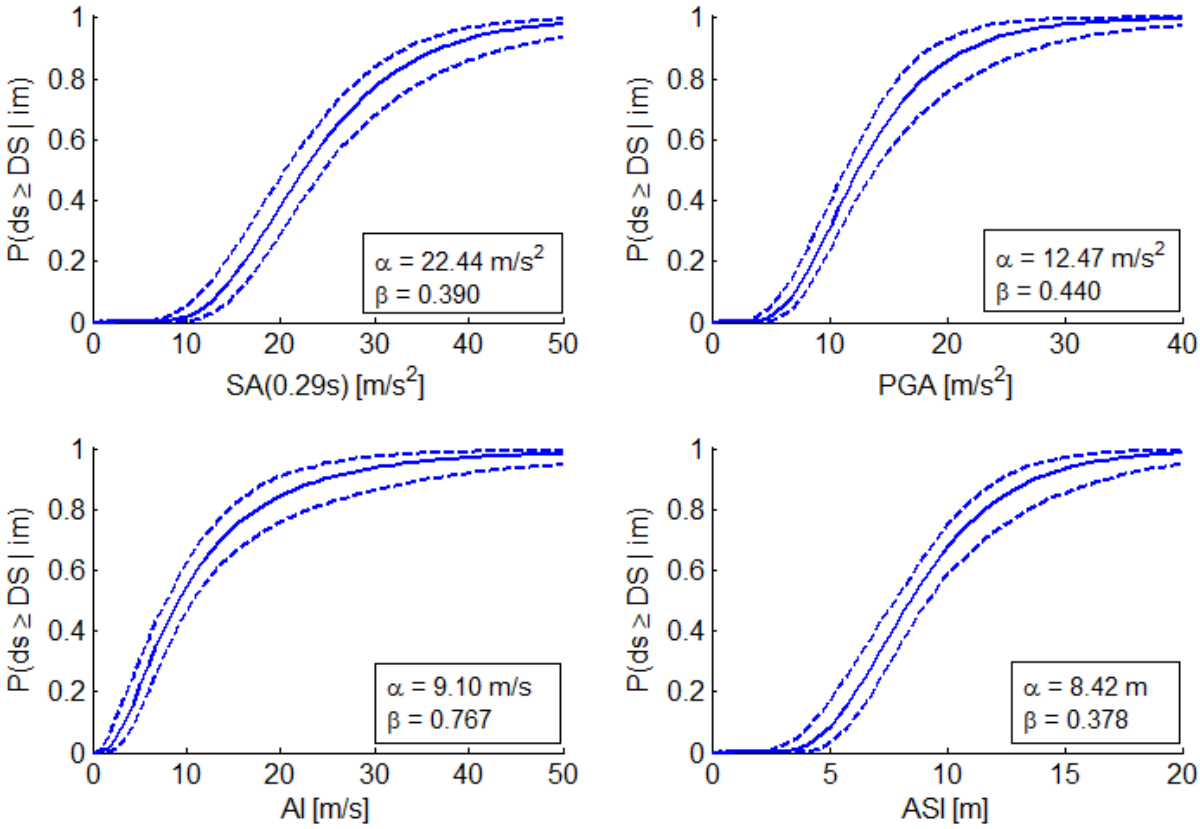

Fig. 9: Fragility curves for the PWR steam line, with respect to various IMs. The solid line represents the median and the dashed lines represent the 5%-95% confidence interval due to the statistical estimation.

4.3.4 Derivation of vector-IM fragility functions

In order to improve the predictive power of the fragility curves and to reduce the dispersion due to the record-to-record variability, it is proposed to combine two IMs and to use this vector-valued predictor for the derivation of the fragility functions. To this end, the following functional form for the damage probability is assumed:

$$\begin{aligned} P_f(im_1, im_2) &= P(ds \geq DS | IM_1 = im_1, IM_2 = im_2) \\ &= \frac{1}{2}[1 + erf(c_1 + c_2 \ln im_1 + c_3 \ln im_2)] \end{aligned} \quad (30)$$

where *erf* is the error function and c_1, c_2 and c_3 are the coefficients to be estimated (i.e., fragility parameters).

A composite variable im_V may then be introduced as follows:

$$im_V = im_1^{\frac{c2}{c2+c3}} \cdot im_2^{\frac{c3}{c2+c3}} \quad (31)$$

Using im_V as the IM, the functional form in Equation 30 is expressed as:

$$
\begin{aligned}
P_f(im_V) &= P(ds \geq DS|IM_V = im_V) = P(ds \geq DS|IM_1 = im_1, IM_2 = im_2) \\
&= \frac{1}{2}[1 + erf(c_1 + c_2\, ln\, im_1 + c_3\, ln\, im_2)] \\
&= \frac{1}{2}\left[1 + erf\left(\frac{\frac{c_1}{c_2+c_3} + ln\, im_1^{\frac{c2}{c2+c3}} + ln\, im_2^{\frac{c3}{c2+c3}}}{\frac{1}{c_2+c_3}}\right)\right] \\
&= \frac{1}{2}\left[1 + erf\left(\frac{ln\, im_V + \frac{c_1}{c_2+c_3}}{\frac{1}{c_2+c_3}}\right)\right] \\
&= \frac{1}{2}\left[1 + erf\left(\frac{ln\, im_V - ln\, \alpha_V}{\beta_V\sqrt{2}}\right)\right]
\end{aligned}
\qquad (32)
$$

where α_V and β_V are the "fragility parameters" of the composite IM im_V, which are finally identified as follows:

$$
\begin{cases}
\alpha_V = \exp\left(-\frac{c_1}{c_2+c_3}\right) \\
\beta_V = \frac{1}{(c_2+c_3)\sqrt{2}}
\end{cases}
\qquad (33)
$$

The coefficients c_1, c_2 and c_3 are estimated with a MLE approach, using the same likelihood function as in Equation 13 (expect that there are now three parameters to find, instead of two).

Thanks to the identification of the "composite" dispersion parameter β_V, it is possible to compute the same three of types of performance metrics, as for the case of scalar-IM fragility curves. More than sixty combinations of vector-valued IMs are tested, and the results for the most promising couples of IMs are detailed in Table 9.

Table 9: Estimation values of the three performance metrics, for different vector-valued IMs. The gray cells indicate the three best performing couples of IMs, for each metric.

IM_1	IM_2	β_V	AIC	AUC
SA(0.14s)	*SA*(0.29s)	0.3724	173.71	0.9568
SA(0.14s)	*SI*	0.3464	167.19	0.9508
SA(0.29s)	*SA*(0.50s)	0.3834	173.74	0.9571
SA(0.29s)	*PGA*	0.3370	161.33	0.9424
SA(0.29s)	*PGV*	0.3718	171.22	0.9591
SA(0.29s)	*AI*	0.4687	171.69	0.9530
SA(0.29s)	*SI*	0.3659	167.43	0.9610
SA(0.29s)	*RSD95*	0.4371	174.11	0.9559
SA(0.50s)	*PGA*	0.3348	158.25	0.9439
PGA	*PGV*	0.3389	166.18	0.9532
PGA	*AI*	0.5027	170.79	0.9468
PGA	*SI*	0.3225	155.43	0.9339
PGA	*ASI*	0.3447	169.06	0.9416
PGV	*ASI*	0.3668	173.61	0.9526

It is found that the vector-valued IMs tend to perform slightly better than the scalar IMs, judging from the values of the three metrics. Some single IMs that were not identified are adequate (e.g., *RSD95*) become much more efficient when combined together. Some examples of vector-valued fragility functions are displayed in Fig. 10, for selected combinations of IMs.

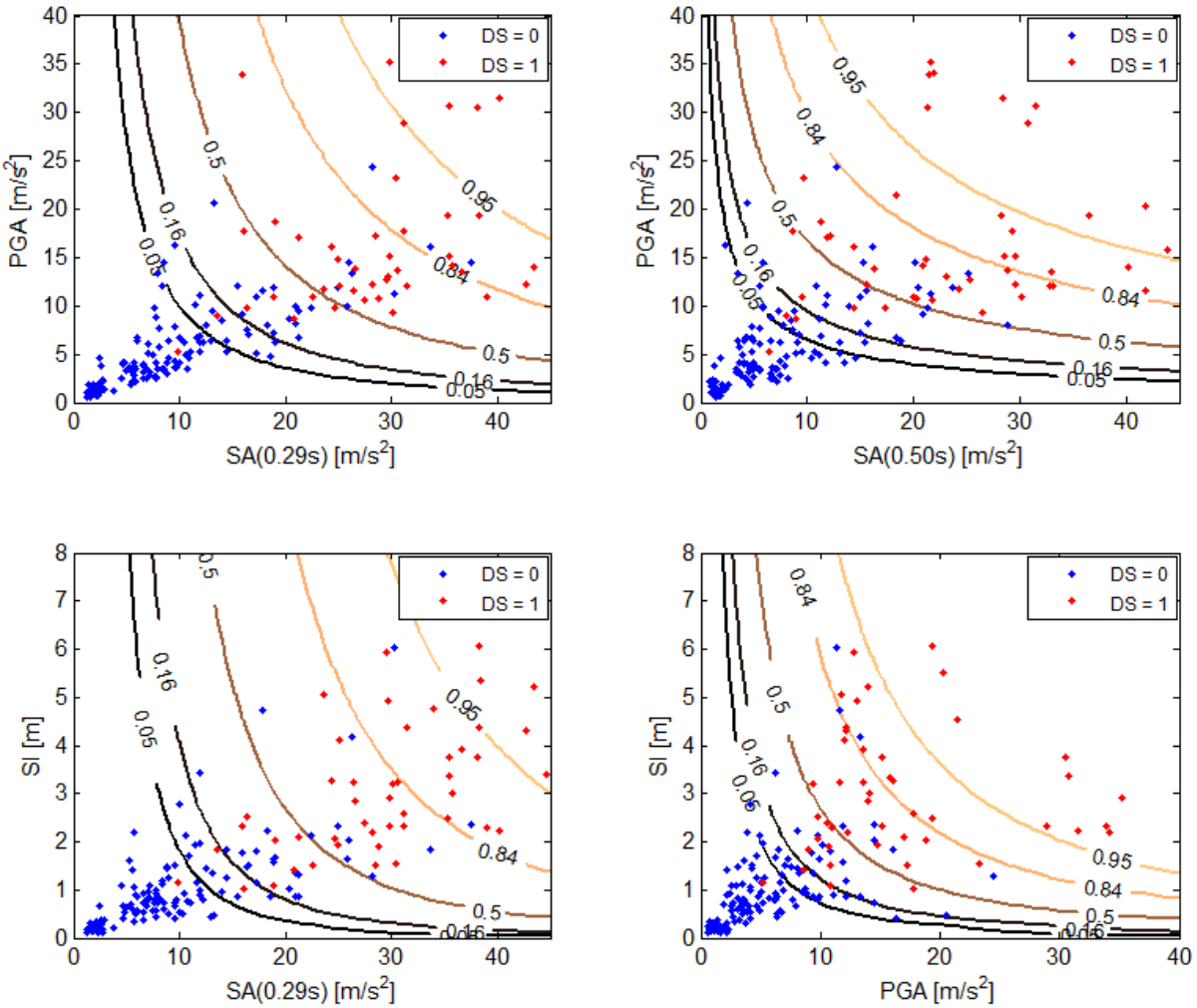

Fig. 10: Iso-probability lines corresponding to some examples of vector-valued fragility function (i.e., probabilities of 0.05, 0.16, 0.5 0.84 and 0.95). The dots represent the outcomes of the NLTHAs in the vector-IM space.

4.3.5 Discussion on uncertainties

The method to perform fragility analysis of a PWR main steam line described in sections 4.3.1-4.3.4, as any other method applicable to such a case, is affected by both epistemic and aleatory uncertainties.

One of the possible sources of epistemic uncertainty is the application of CAST3M model (Rahni et. al. 2017), which is a typical situation when any model is applied to describe physical processes. The analysis of the uncertainty of the model would demand special studies and, in principle, should be performed together with sensitivity analysis in order to find the input parameters which can the most affect the results. Formally this can be achieved by using different sensitivity analysis techniques (e.g., Iooss & Lemaitre, 2015), by following either a local approach (i.e. where the effect of a single parameter on the final output is investigated one-at-a time) or global (i.e. the effect of a specific uncertainty to the overall uncertainty in the output° for example, Sobol' variance-based indices (e.g. Saltelli et al., 2008) describing which portion of the uncertainty (expressed in terms of the ratio of conditional variance to total variance) comes from the investigated parameters or input data. Note that global sensitivity analysis techniques could also be used for assessing the importance of each IMs and possibly guide the selection of the most informative ones. However, this approach still would not cover all the epistemic uncertainties and it seems that expert judgment would be necessary in any case.

The selection of seismic input for non-linear time-history analyses finally led to 180 total ground motion records. From statistical point of view such an amount is usually satisfactory, however it should be noted that 30 records are used for each scaling level, which means that one can expect less accuracy in estimating conditional mean spectrum.

Similarly as for CAST3M model, the OpenQuake engine is used to perform hazard disaggregation in the process of the seismic input selection, hence the same general comments can be applied if epistemic uncertainties are considered.

Occurrence of damage state is defined arbitrarily at EDP_{th} = 400 kN for maximum transient stress – the choice of this value can be potentially also a source of uncertainty. In such a case simple sensitivity analysis could be performed, but taking into account that epistemic uncertainties are associated with the models applied, this seems to lead to the effects of lower order.

Derivation of scalar-IM fragility functions is based on three performance metrics estimating the adequacy of potential IM. One of the metrics is a standard deviation of the fragility curve thus explicitly related to the uncertainty. For vector-valued IM the same metrics have been applied and it has been found that application of two properly chosen intensity measures produces the lower uncertainty than application of any single IM. Basically, this type of analysis can be extended to the application of three or more IMs, which, in principle, could lead to further decrease of uncertainty, however the adequate combination of IMs would be more difficult. In this respect, one of the points is the proper estimation of the coefficients c_1, c_2 and c_3 (or more if more IMs are taken into account). For the maximum likelihood estimation applied for this estimation, in principle the Rao-Cramer inequality can be used to give the lower bound of the mean square errors of the estimators. Then the uncertainty of fragility parameters α_V and β_V can be also estimated.

The other possible choice could be the application of minimum variance estimator – in this case it is important (according to Rao-Blackwell theorem) to find complete sufficient statistics of estimating variables, which in case of complex system would be a great challenge.

Whatever method is used, one should have still in mind, that there are sources of epistemic uncertainties not easy to handle as described in section 3.5 and, for this reason, expert judgment cannot be disregarded.

Following this qualitative analysis of potential uncertainty sources, it is proposed to discuss a set of procedures for the quantitative estimation of some uncertain components, namely the record-to-record variability, the uncertainty due to the number of data points, and the in-situ variability due to the variability of mechanical and geometrical parameters.

a. Decomposition of the record-to-record variability

The contribution of the record-to-record variability to the global uncertainty structure may be estimated thanks to the comparison between scalar-IM fragility curves and vector-IMs fragility surfaces. To this end, as an example, it is proposed to reduce the fragility surface w.r.t. [*PGA* ; *SA*(0.29s)] (see top left plot in Fig. 10) into a fragility curve w.r.t. *SA*(0.29s) only. This operation should consider the correlation between the two IMs, in order to preserve the hazard consistency of the applied loading. Therefore, a first step consists in estimating the distribution of the secondary IM (i.e, *PGA*) w.r.t. *SA*(0.29s), using the dataset of the input ground-motion records: a median line and its 16%-84% confidence intervals is then plotted (see Fig. 11, left). The space delimited by this interval provides also practical guidance on the validity domain of the fragility surface, in the sense that it identifies the IM combinations that are very unlikely.

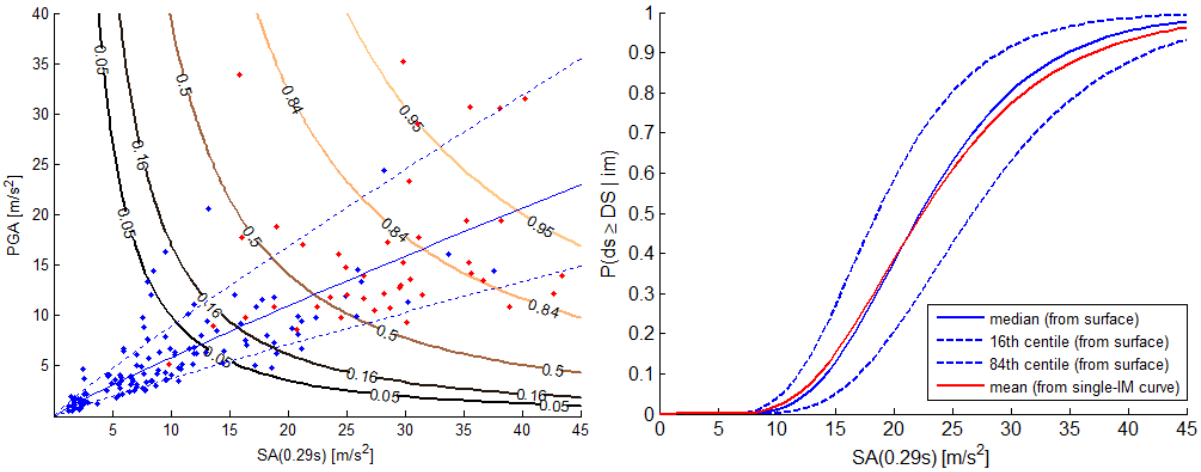

Fig. 11: Left: fragility surface w.r.t. PGA and SA(0.29s), the solid blue line represents the median of the PGA-SA(0.29s) distribution and the dashed blue lines the 16%-84% confidence intervals; Right: Equivalent fragility curves w.r.t. SA(0.29s).

It is then proposed to generate "slices" of the fragility surfaces by following the distribution of *PGA* as a function of *SA*(0.29s) (i.e., solid and dashed lines in Fig. 11, left). As a result, the "slices", now represented as a function of the unique IM *SA*(0.29s), may be compared to the original scalar-IM fragility curve taken from Fig. 9. The fragility curves in Fig. 11 right are identified as follows:

- *Solid red line*: "mean" fragility curve corresponding to the scalar-IM fragility curve;
- *Solid blue line*: median fragility curve corresponding to the "median" slice of the fragility surface;
- *Dashed blue lines*: 16%-84% confidence intervals around the median fragility, corresponding to the lower and upper bounds of the slices of the fragility surfaces.

Finally, this family of fragility functions corresponds to the probabilistic framework by Kennedy et al. (1980), which has been detailed in section 3. The mean fragility curve, w.r.t. to *SA*(0.29s), has a total standard deviation β_{tot} = 0.390. Meanwhile, the median fragility curve, obtained from the fragility surface w.r.t. *PGA* and *SA*(0.29s), has a standard deviation of 0.342, which actually corresponds to the aleatory randomness term (i.e., β_R). The confidence intervals obtained from the graphical construction in Fig. 11 are then used to estimate the epistemic uncertainty term, i.e. $\beta_U \approx 0.187$.

It may be concluded that the vector-IM fragility functions lead to the transfer of a part of the record-to-record variability into a form of epistemic uncertainty, which is related to the description of the seismic loading given the hazard at the specific site.

b. Uncertainty due to the number of data points

The epistemic uncertainty due to the number of data points in the simulations, i.e. related to the quality of the statistical estimation of the fragility parameters, may also be evaluated in the case of vector-IM fragility functions. To this end, the same bootstrap approach as in section 4.3.3 is applied to the fragility surface w.r.t. of *PGA* and *SA*(0.29s). The outcomes of the bootstrap sampling are displayed in Fig. 12, in the case of 5%-95% confidence intervals.

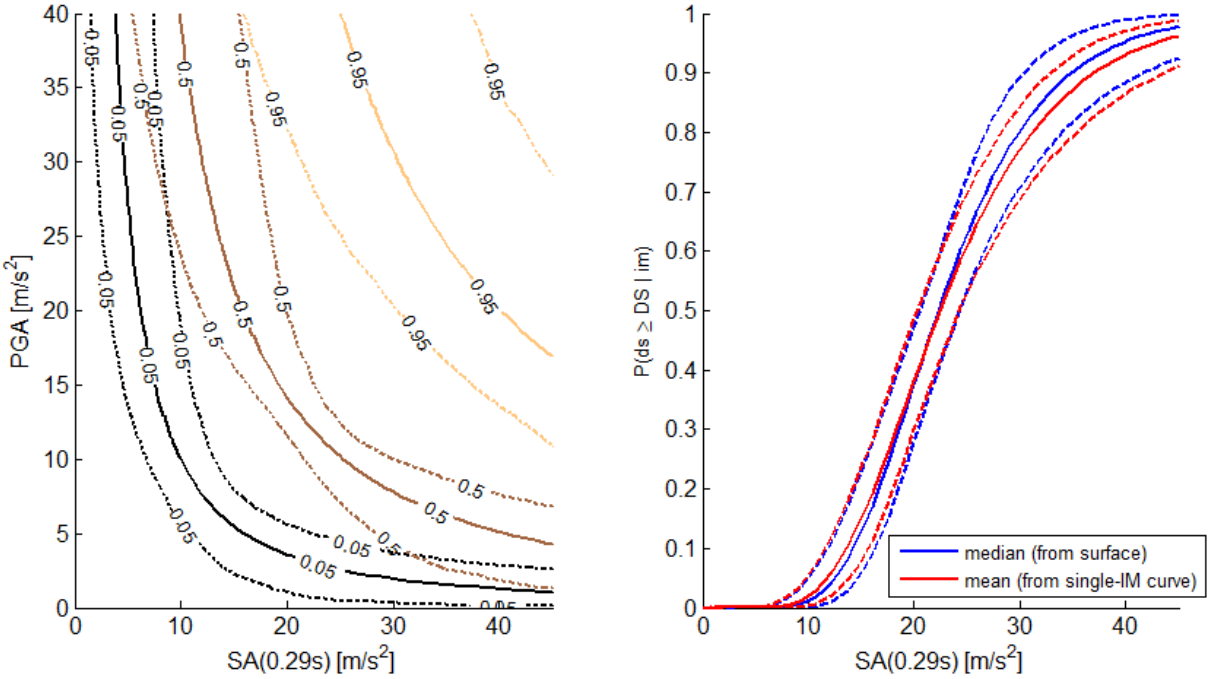

Fig. 12: Left: fragility surface w.r.t. PGA and SA(0.29s), with the 5%-95% confidence intervals (dashed lines) due to the statistical estimation; Right: Equivalent fragility curves w.r.t. SA(0.29s) and related 5%-95% confidence intervals due to the statistical estimation.

In Fig. 12 left, the confidence intervals around the iso-probability lines are narrower around the locations where the most data points are present, as expected. In order to compare these confidence intervals with the ones estimated for the corresponding single-IM fragility curves (i.e., Fig. 9 top left), the fragility surface is reduced to a scalar case w.r.t. *SA*(0.29s) only, following the same approach as before (i.e., use of a "median" slice of the fragility surface). The curves in Fig. 12 right reveal a similar order of magnitude for the confidence intervals due to the amount of data points, both for the single-IM fragility curve and the vector-IM fragility function.

c. In-situ uncertainty due to the variability of mechanical and geometrical parameters

The *in-situ* uncertainties (see classification in section 3.5) related to the mechanical and geometrical parameters of the main steam line (e.g. elastic stiffness, damping, pipeline thicknesses, etc) were studied by randomly sampling them using the Latin Hypercube Sampling method (McKay et al., 1979). This method enables us to cover a broad range of situations (space-filling sampling method), i.e. it provides good representativeness of reality at a reasonable number of sampled situations and therefore was chosen. Orthogonal sampling could be another choice, then however the difficulty would come from *a priori* division of the sampling space. As a result, in total 360 models of the PWR structure have been built.

The influence of the random mechanical and geometrical parameters was studied by testing whether they should be integrated in the vector-based fragility model. Formally, we test whether the mean and variance of the multivariate lognormal model (Equation 30) should be completed by a sum of univariate functions of the mechanical and geometrical parameters. This problem is solved within the setting of Generalized Additive Model for Location, Scale and Shape parameter (GAMLSS; Rigby & Stasinopoulos, 2005) so that the functions of the uncertain parameters are assumed to be represented by univariate, non-linear and smooth termed as GAM (here modelled by P-splines). Here we restrict the analysis to a semi-parametric additive formulation as follows:

$$\theta = \beta_0 + f_1(im_1) + f_2(im_2) + \sum_{j=1}^{p} f_j(x_j) \quad (34)$$

Where θ is the parameter of the lognormal model (either the mean or the variance); $im_{1,2}$ are the intensity measures (*PGA* and *SA* at 0.29s); x_j are the p mechanical and geometrical parameters (here, p = 10); f_j corresponds to the GAM (here, P-spline models); and β_0 is a constant. Due to the limited number of models (here, 360), the maximum-likelihood-based fitting of this model is combined with a penalization procedure (Wood et al., 2016), which allows setting to zero the variables of negligible influence in the GAMs.

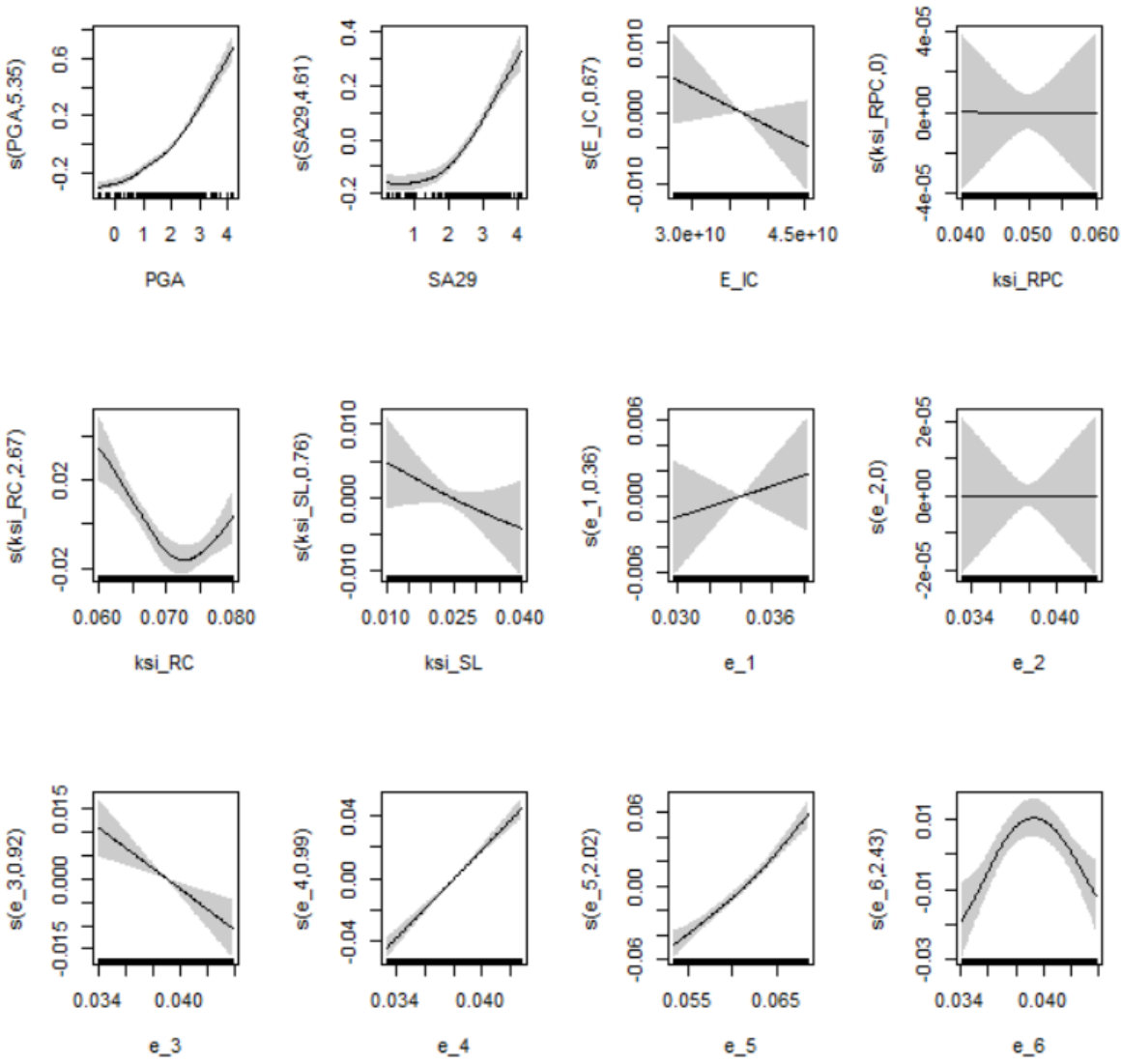

Fig. 13: Smooth models showing the evolution of the mean component of the log-normal vector-based fragility model as function of the input parameters, namely the intensity measures are the PGA and SA at 0.29s(denoted SA29), and the mechanical and geometrical parameters; horizontal trends indicate negligible influence of the corresponding parameter.

Fig. 13 shows the evolution of the mean component of the lognormal vector-based fragility model depending on the intensity measures (*PGA* and *SA* at 0.29s) and on the mechanical and geometrical parameters. We see that the pipe thickness e_2 has negligible influence: the penalisation leads to a constant trend at zero. We also note the very slight influence of e_1, and of ξ_{RPC} (small evolving tendency).

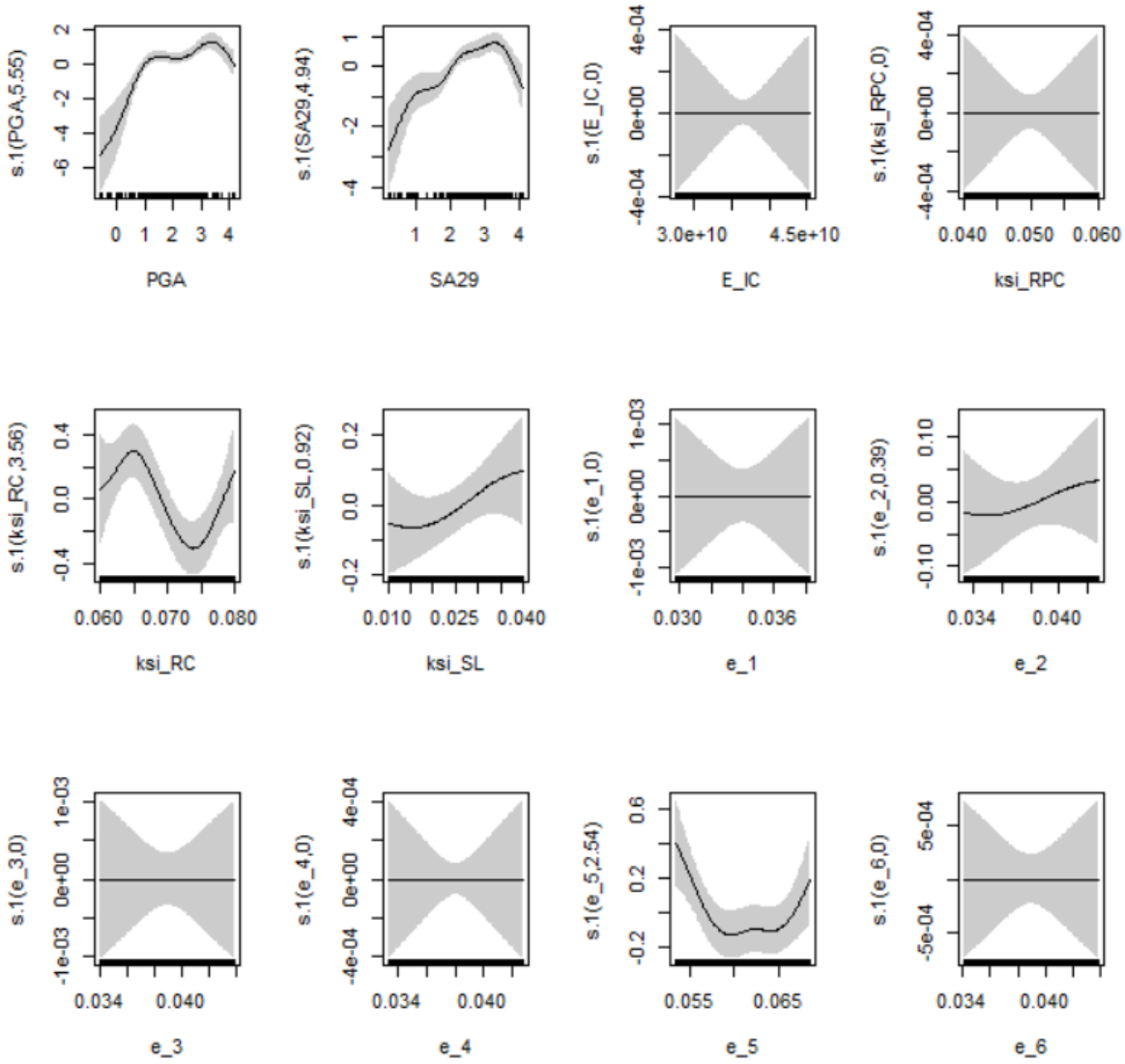

Fig. 14: Smooth models showing the evolution of the variance component of the log-normal vector-based fragility model as function of the input parameters, namely the intensity measures are the PGA and SA at 0.29s (denoted SA29), and the mechanical and geometrical parameters; horizontal trends indicate negligible influence of the corresponding parameter.

Fig. 14 gives a similar analysis but for the variance parameter of the fragility model. Here we can note the negligible influence of two mechanical parameters, E_{IC} and ξ_{SL}, and of four thickness parameters e_1, e_3, e_4 and e_6 on the variance.

One major interest of the procedure is the ability to study the evolution of the full probability distribution of *EDP* as a function of the selected parameters and to identify regions of the parameters' values leading to large failure probability. Fig. 15 illustrates this type of analysis by focusing on the fourth thickness parameter e_4. The blue envelope is the envelope of all CDFs derived from the random sampling of all parameters. The red one includes the impact of all random parameters, except for e_4, whose value is fixed at a constant value ranging from 0.05 to 0.07. We note the rightwards translation of the red envelope when increasing e_4, which indicates that the larger e_4, the larger the damage probability i.e. Pr(EDP_{th} ≥ 400 kN).

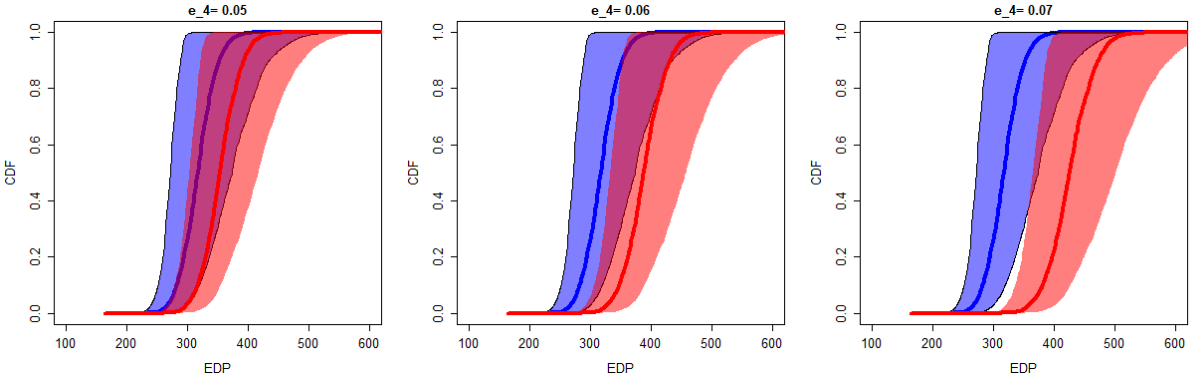

Fig. 15: Evolution of the CDF related to EDP when the pipe thickness parameter varies. The blue envelope is the envelope of CDFs derived from the random sampling of all parameters. The red one includes the impact of all random parameters, except for e_4, whose value is fixed at a given value ranging from 0.05 to 0.07.

4.4 Application: Fragility analysis of a fuel assembly grid

As another illustrative example a fragility surface for fuel assemblies is estimated, taking into account the seismic loads only.

The virtual reactor as defined in NARSIS project contains 241 closely spaced fuel assemblies, which are slender structures supported at both ends. Fuel assembly geometry and core pattern are illustrated in Fig. 16. Colored positions are positions equipped with Rod Cluster Control Assembly (RCCA).

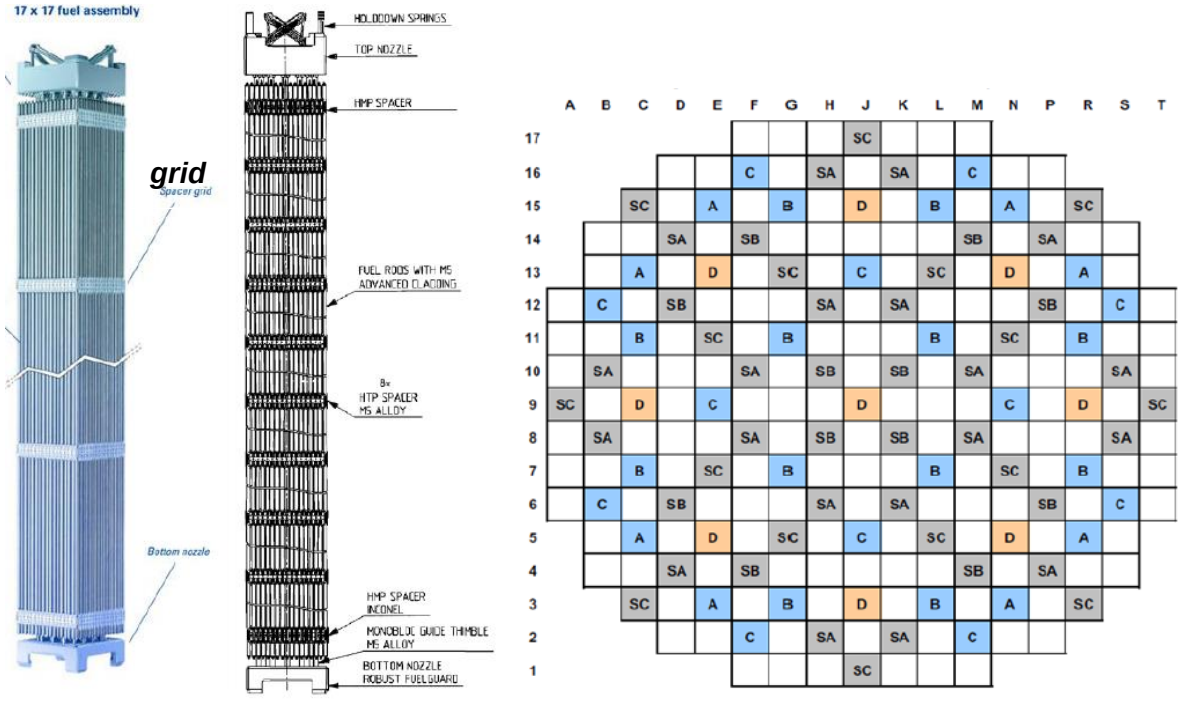

(a) Fuel geometry *(b) Core pattern*

Fig. 16: 17x17 fuel assembly and core pattern

During an earthquake, fuel assemblies are likely to impact to each other or to the core baffles at the grid level. Impact loads should not lead to an excessive inelastic grid deformation, which would prevent regular insertion of the Rod Cluster Control Assemblies (RCCA) in case of a reactor trip.

In order to estimate the impact loads, 2D models of rows of Fuel Assemblies (FA) are built. The fuel assemblies are modelled by linear beams coupled at the top and at the bottom to the motions of the grid plate and the lower core plate, respectively. These FA are rather flexible structure. Their first Eigen frequency is lower than 3 Hz. Interaction of adjacent FA is modeled by nonlinear elastoplastic impact couplings between the spacer grid impact nodes attached to the beams. This model is able to predict residual deformations induced by an earthquake, which can be compared to criteria that define acceptable grid deformations with regard to RCCA drop.

The 180 ground motion time histories, defined in section 4.3.2, are propagated through a building model of the reference plant. The building time histories at the core level are applied directly (without considering the dynamic behavior of the RPV internals) to the 2D model of the FA rows and for each time history, it is evaluated whether failure occurs.

In a first step, univariate fragility curves are built for several intensity measures.

The parameters of the classical lognormal fragility model are identified using Maximum Likelihood estimation, on the basis of 90 time histories randomly chosen within the initial set of 180 time histories. Then, in order to identify which IM performs best for this test case, a Receiver Operating Characteristics (ROC) analysis is performed on the basis of another set of 90 time histories. The operation is repeated several times with different sets of 90 time histories in order to check the robustness of the results. This step permits to identify, without a-priori assumptions, the best performing IM for this given test case. Fig. 17 shows the results obtained for the most efficient IM. According to the ROC curves *(b)*, the most efficient IM are *ASI* and *SrVI*. This is also indicated by the fact that the corresponding fragility curves *(a)* are steeper than the ones based on other IM; a steeper fragility curve implies less uncertainty about the capacity, i.e. the level of the IM at which failure occurs.

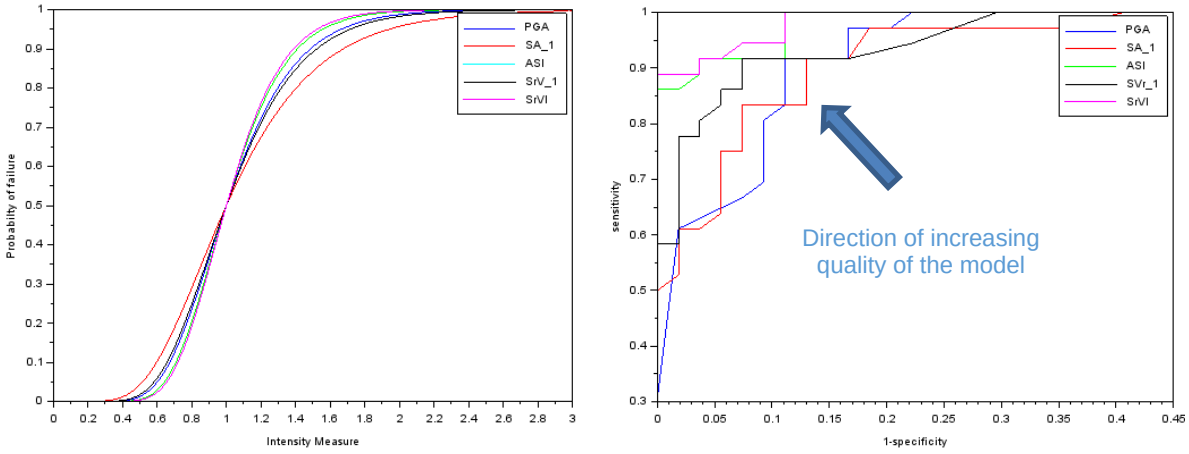

(a) Fragility models (Normalized Fragility curve. Median Capacity equals 1) *(b) ROC analysis*

PGA: peak ground acceleration

SA_1: Absolute spectral acceleration at first frequency (f1) of the fuel assembly

ASI: average absolute spectral acceleration in the range [f1: f1+1Hz]

SVr_1: Relative spectral acceleration at first frequency (f1) of the fuel assembly

SrVI: average relative spectral velocity in the range [f1: f1+1Hz]

Fig. 17: Results of the fragility function considering one intensity measure

In a second step, it is studied whether uncertainties can be reduced by building a bivariate fragility surface based on two uncorrelated (or poorly correlated) IMs. No pair of IM including *ASI* or *SrVI* has led to a reduction of uncertainty in comparison with *ASI* or *SrVI* alone.

However, it was found that it is possible to reduce uncertainties regarding the capacity in terms of *PGA* alone by building a vector-valued fragility surface that combines *PGA* and the ratio *PGA*/*PGV* (peak ground velocity). These two parameters are poorly correlated, and *PGA*/*PGV* is a good indicator of spectral shape.

Fig. 18 shows the effect of the second IM, PGA/PGV, by plotting fragility curves keeping the second IM constant and comparing with the univariate fragility curve based on *PGA*.

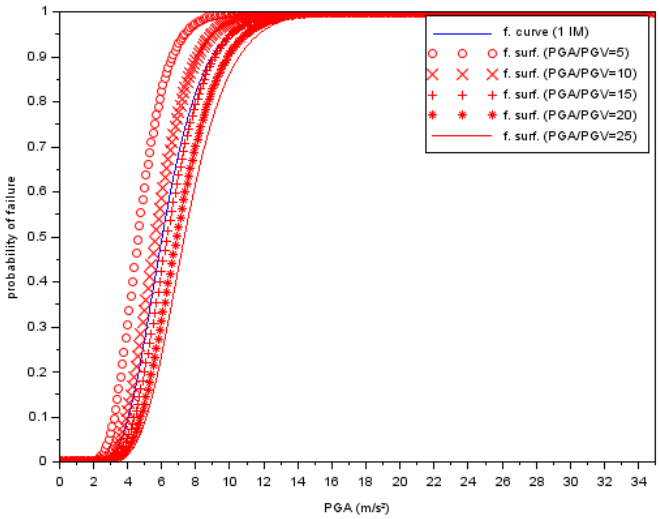

Fig. 18: Single-variable fragility curve compared to slices of a fragility surface

To conclude, the fragility surface representing ground motion by {*PGA* and *PGA*/*PGV*} tends to reduce uncertainties in comparison to the fragility curve representing ground motion only by {*PGA*}. It seems equivalent to a fragility curve representing ground motion by a parameter that is specific to the structure (e.g. *ASI* → spectral acceleration around its first frequency).

A sensitivity analysis should be performed to evaluate whether the dynamic response of the RPV internals – not considered in the present study – has significant effects on the presented results.

5 Vector-Valued IMs for the Treatment of Multi-Hazard Interactions

This section is devoted to the case of fragility functions that account for multiple hazard functions. After a literature review of existing fragility models that may be relevant for nuclear applications, a short reflexion on potential frameworks for the multi-hazard fragility modelling of SSCs is proposed.

5.1 Literature Review

Multi-hazard interactions have been addressed in detail within the FP7 ASAMPSA_E project (Decker & Brinkman, 2016), which should constitute the starting point for the multi-hazard fragility analyses in NARSIS. Moreover, the literature on interactions in terms of multi-risk frameworks has been reviewed as part of NARSIS deliverable report D1.1 (Daniell et al., 2018).

System theory matrix approaches are suggested as a tool to consider hazard interactions and time-variant vulnerability. Literature along these lines was introduced in Liu et al. (2015) with these methods having been used in various fields including environmental issues (e.g. Simeoni et al., 1999; de Pippo et al., 2008), rock engineering (e.g. Hudson, 1992) and natural hazard assessment (Kappes et al., 2010; Mignan et al., 2014; Gill & Malamud, 2014). The basis of this approach consists of the comprehension and description of the relationships among agents and processes in the evolution of the system (Liu et al., 2015).

As part of the MATRIX project, Garcia-Aristizabal et al. (2013) provided more detail on multi-risk approaches; however as of 2011, it was detailed that no studies had used extensive multi-hazard assessment. Since 2011, literature has explored this in greater detail with a number exploring comprehensive multi-hazard risk assessment (Marzocchi et al., 2012; Selva, 2013; Mignan et al., 2014). Marzocchi et al. (2012) studied multi-hazard risk via event trees for the triggering effects in Italy: they examined the fact that individual events modelled separately may not directly permit the creation of a combined risk and the dependence between hazards needs to be taken into account.

The MATRIX project set out to develop methodologies and concepts in multi-hazard and the associated three-level framework (Liu et al., 2015) for multi-risk assessment gave a first framework for how to deal with time-variant vulnerability as well as the hazard interactions within a singular event between perils. Within the MATRIX project, event-tree and fault-tree strategies were used for various case studies – Cologne for earthquake-triggered embankment/flood defence failures; Guadeloupe for rainfall and earthquake-induced landslide events; Naples for volcanic earthquakes and seismic event triggered by volcanoes.

Gill & Malamud (2014) also examined over 20 hazards with a matrix approach similar to Level 2 of the MATRIX approach. A number of other approaches in addition have been presented to attempt a solution for multi- hazard analysis (Liu et al. (MmhRisk-HI), 2017), among others attempting multivariate approaches to assess multiple parameter distributions and correlations for hazard analysis (Sadegh et al., 2018).

Selva (2013) has also proposed a probabilistic framework for the statistical treatment of multi-risk interactions. Functional forms are introduced for the quantification of all types of interactions (i.e. in terms of hazard, exposure and fragility), while various risk factors are defined in order to identify the different types of contributions from the multiple hazards. The concept of the time window, during which the effects of multiple hazards are still present on a given asset, is recognised as a key parameter of multi-risk analyses: this feature appears to be essential especially when considering concurrent independent hazard events.

As summarised in Fig. 19, the multi-risk assessment framework by Marzocchi et al. (2012) allows for the treatment of either independent or cascading events, as long as the space and time boundaries of the problem at hand are properly specified. The use of harmonised loss metrics (e.g., based on functionality or performance loss in the case of technical systems such

as NPPs) is necessary in order to the aggregate the effects of the various hazard combinations.

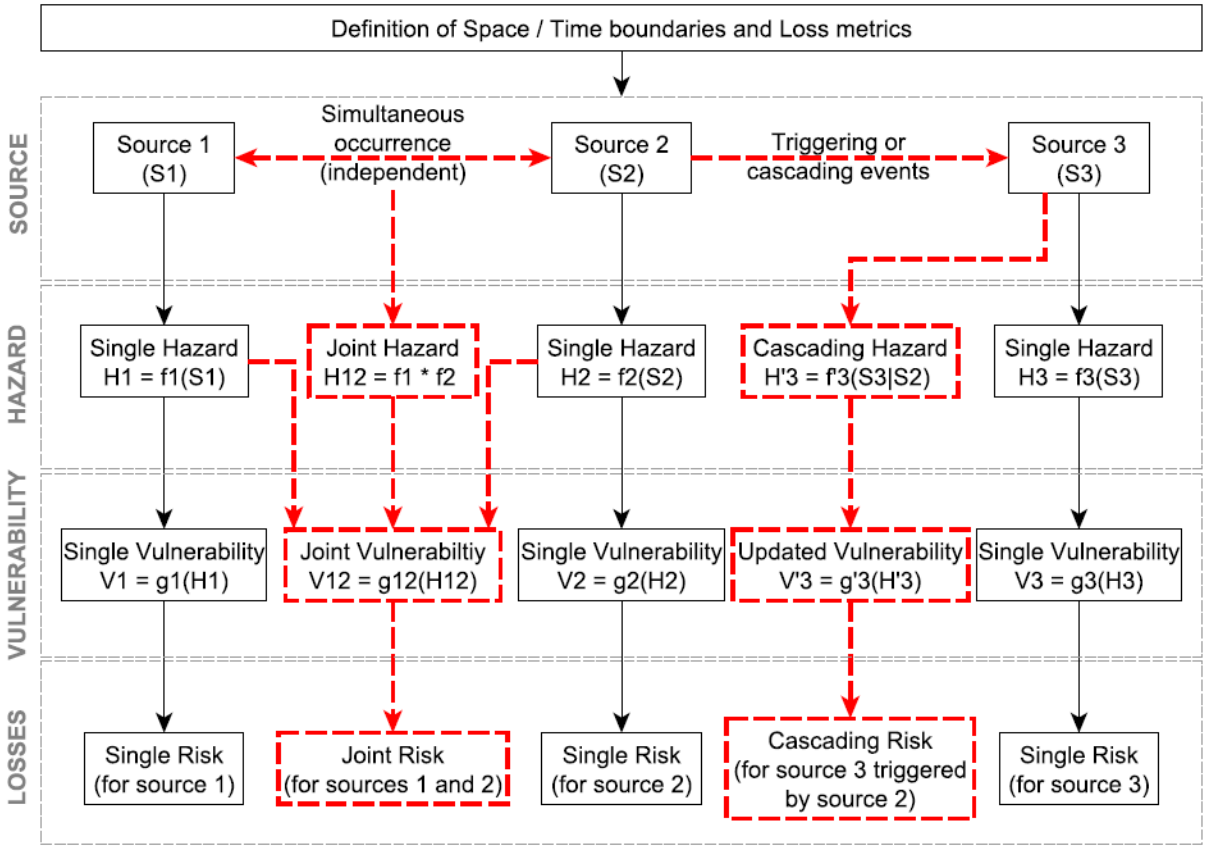

Fig. 19: Multi-risk assessment framework proposed by Marzocchi et al. (2012), for joint independent hazards (sources 1 and 2) and cascading hazards (source 2 triggering source 3)

Whatever the multi-hazard framework considered, *ad hoc* fragility models must be developed in order to translate the cumulative or joint effects of multiple loadings into updated probabilities of damage or failure (e.g, joint or updated vulnerability models in Fig. 19).

A review within NARSIS report D1.1 (Daniell et al., 2018) examined the following interaction components:-

- Longer term effects of induced natural hazards have been investigated by Cavalieri et al. (2016) following the Tohoku and Christchurch earthquakes of 2011, where time in between events as well as damaged infrastructure caused issues for coincidental hazards. The multi-hazard aspects in this case were not concurrent (although secondary effects and aftershocks were of course also part of these sequences), but the main issue was the damage to pipelines, dams and flood retention structures which then affected the impact of the flood hazard due to extreme rainfall (observed in 2014 in the case of Christchurch), where major flooding of the city occurred.
- A significant number of authors have examined earthquake interactions with volcanic eruptions and triggered earthquakes (Feuillet et al., 2005; Neri et al., 2013, Bonini et al., 2016), however very few modelling frameworks have been presented. Zuccaro et al. (2008) presented one with the interaction of the component hazards from earthquake and volcanic eruptions.
- Butler et al. (1991) examined landslide-induced floods historically. Crosta & Frattini (2003) and Chen et al. (2016) have explored such events from the other perspective with rainfall-induced slope failures.

- On the flood modelling side, multi-variate flood damage assessment has been explored by a number of authors, where the correlation of flow, velocity, depth and duration has been explored. Kreibich et al. (2009) explored the correlation to damage with later authors such as Merz et al. (2013), Chinh et al. (2015) exploring the relationship through multi-variate distributions.
- Nielsen et al. (2015) describe 68 Tornado and Flash Flood events (TORFF) occurring simultaneously between 2008 and 2013; simultaneous occurrences have also been described by Rogash and Racy (2002) in 31 events from 1992 and 1998. Events such as this cause many problems for humans given the lack of safe options for sheltering from both a high wind and flash flood.
- Phan et al. (2007) used SLOSH models to estimate wind speeds and storm surge heights creating site-specific joint distributions. On the hazard side, other authors have followed the same combination such as Lin and Vanmarcke (2010), however they have also accounted for the vulnerability due to combinations.
- Li et al. (2011) and Pita et al. (2012) have both created methodologies to account for rain and wind damage co-occurring during hurricanes with joint statistical distributions. Mudd et al. (2016) undertook a numerical simulation behind a joint probabilistic analysis of hurricane winds and rainfall. Flood and sea-level rise combinations have been examined by many researchers but is of little impact for NPPs, Nicholls et al. (1999) and Hinkel et al. (2014) are two such studies.
- A coupled model has been used to model interactions between hazards by adjusting the relative property by Dietrich et al. (2010) for riverine flood, wind, storm surge, tidal effects and wind wave effects.
- Tyagunov et al. (2018) provide a multi-hazard fragility and failure probability analysis for fluvial flood control structure systems using earthquake and flood prone areas and the influence of liquefaction. Their failure probability is described by a three-dimensional fragility surface as a function of both earthquake ground shaking (PGA) and floodwater level (impoundment of the dike), however does not use additional parameters within any one of the peril types. Tyagunov et al. (2018) showed that a rise in floodwater level reduces the liquefaction triggering PGA threshold due to high moisture content in the dike core.
- The OOFIMS framework (Franchin & Cavalieri, *n.d.*) has also been advanced by Cavalieri et al. (2016) for various multi-hazard scenarios including that of earthquake and flood.
- When considering earthquake and flood hazard and the developed fragility curves, the liquefaction potential is important with the non-zero liquefaction probability for an exemplary dike location becomes evident. Non-structural elements and their damageability are brought into Venanzi et al. (2018) exploring wind and seismic loads on tall buildings.
- The impact of aftershocks in terms of vulnerability is distinctively different to mainshocks since they usually occur in the same area where the mainshock occurred, yet with a smaller amount of shaking. Pre-damaged buildings are more vulnerable (e.g. Wen et al., 2017). Past events have shown various times how relevant the aftershock impact on a risk level can be (Shome & Williams, 2014).
- Ribeiro et al. (2014) and Song et al. (2016) presented a framework for mainshock-aftershock sequence modelling of steel structures, both showing significant effects due to aftershocks.

The past few years have seen the developments of specific multi-hazard fragility models that correspond to some of the aforementioned interactions. A non-exhaustive summary is provided in Table 10.

Table 10: Summary of some recent studies devoted to the development of multi-hazard fragility models.

Study	Hazard(s)	Exposed element(s)	Intensity measure	Main features
Lee & Rosowsky (2006)	earthquake, snow	wood frame building	PGA, snow load on rooftop	numerical simulations, parametric fragility (different snow loads)
Kafali (2008)	wind, wave effects	offshore platform	wind speed over sea surface, wind angle	analytical solution, crossing theory for system fragility, linear oscillator approximation
Zuccaro et al. (2008)	explosive volcanic eruption (earthquake, ash-fall, pyroclastic flow)	residential buildings	macroseismic intensity, ash load, dynamic pressure	empirical / expert-based vulnerability functions, updated Damage Probability Matrices, sequence of events
Asprone et al. (2010)	blast, earthquake	RC building	load factor, SA(T)	numerical simulations, independent fragility curves, aggregated annual collapse probabilities
Chiodi et al. (2011)	earthquake, wind	steel hangar structure	SA(T), wind speed	methodological framework, hazard-independent fragility
Li et al. (2011)	wind, storm surge (hurricane)	residential buildings		
Alipour & Shafei (2012)	earthquake, riverine flood (scour)	RC bridge	PGA, scour depth (from flow discharge and flow depth)	numerical simulations, parametric fragility (different scour conditions)
Li & van de Lindt (2012)	wind, flood earthquake, snow	residential buildings	wind speed, water depth, SA(T), snow load	hazard-independent fragility curves, harmonized losses
Pita et al. (2012)	rainfall, wind (hurricane)	residential buildings	wind speed, rain rate	numerical simulations, building component damage curves due to wind (roof, gable, windows, doors), damages curves due to water ingress
Prasad & Banerjee (2013)	earthquake, riverine flood (scour)	RC bridge	PGA, scour depth (from flow discharge and flow depth)	numerical simulations, parametric fragility (different scour conditions)
Kameshwar & Padgett (2014)	earthquake, storm surge (hurricane)	highway bridges	PGA, surge, water depth	numerical simulations, multivariate GLM, hazard-independent fragility, risk comparison
Ribeiro et al. (2014)	earthquake (aftershocks)	steel structure	SA(T) for mainshock and aftershock	numerical simulations, back-to-back NLTHAs, conditional probability of failure during aftershock given mainshock, robustness index
Charvet et al. (2015)	tsunami, debris impact	wood / masonry / RC / steel buildings	water depth, flow velocity, impact	empirical fragility (data from 2011 Great East Japan tsunami), multivariate GLM
Yilmaz (2015)	earthquake, riverine flood (scour)	highway bridges	PGA, occurrence of	numerical simulations, component- and system-level fragility

			characteristic flood event	
Bodda et al. (2016)	earthquake, flood	flood defense structure (gravity dam)	PGA, water depth	numerical simulations, modelling of seepage through foundation, fragility surface
Cavalieri et al. (2016)	earthquake, flood (rainfall)	storm water system	PGV, PGD, flow discharge	numerical simulations (OOFIMS), effects of earthquake damage on the subsequent flood hazard
De Risi et al. (2017)	tsunami	wood / masonry / RC / steel buildings	water depth, flow velocity	empirical fragility (data from 2011 Great East Japan tsunami), multivariate GLM
Gehl & D'Ayala (2016)	earthquake, riverine flood	RC bridge	PGA, flow discharge	numerical simulations, system reliability
Song et al. (2016)	earthquake (aftershocks)	steel structure	SA(T) for mainshock and aftershock	numerical simulations, back-to-back NLTHAs, aggregation of mainshock-aftershock losses
Goda and De Risi (2018)	earthquake, tsunami	residential buildings	PGV, water depth	empirical fragility, hazard-independent fragility, aggregation of losses
Tyagunov et al. (2018)	earthquake (liquefaction), riverine flood	fluvial dike	PGA, water depth	numerical simulations, computation of liquefaction potential , fragility surface
Venanzi et al. (2018)	earthquake, wind	tall building	SA(T), wind speed	numerical simulations, hazard-independent fragility curves, aggregated annual losses

5.2 Proposed multi-hazard fragility framework for NPP applications

The above literature review has made apparent that a wide range of cases should be considered when deriving multi-hazard fragility models: these rely on many factors, such as the simultaneous or sequential occurrence of hazards loadings, the use of single or multiple correlated IMs, the failure mechanisms considered for the computation of losses, etc. Moreover, in the case of NPPs, the fragility models for SSCs should provide useful information on the functionality of the elements, so that they can be directly integrated into the subsequent risk analysis tools (i.e., PSA framework). Therefore, the following decomposition of the chain of events leading to potential functionality loss is proposed:

- *Hazard event*: it represents the hazard type that is susceptible to induce external loadings to the studied SSC.
- *Intensity measure*: it represents quantifiable measures of the considered hazard type, i.e. the input variables of the fragility model. As seen in the case of earthquakes, a single hazard may generate multiple IMs.
- *Physical failure mode*: it represents the damage mechanisms of the SSC, which can be evaluated through a set of physical variables (i.e., engineering demand parameter). These failure modes may vary according to the hazard type considered, so that each failure mode is linked to one or several specific IMs.
- *SSC functionality state*: it represents the outcome of the fragility model, which should be able to predict whether the SSC will be able to perform its intended function or not.

Several physical modes of a given SSC may be combined in order to assess its functionality.

Following this decomposition, five main cases for fragility assessment are identified (see Fig. 20), depending on the complexity of the application. It is believed that these five cases are able to cover most of the multi-hazard cases, although cases #4 and #5 may be further refined into several sub-cases (e.g., distinction between correlated, cascading or independent hazards).

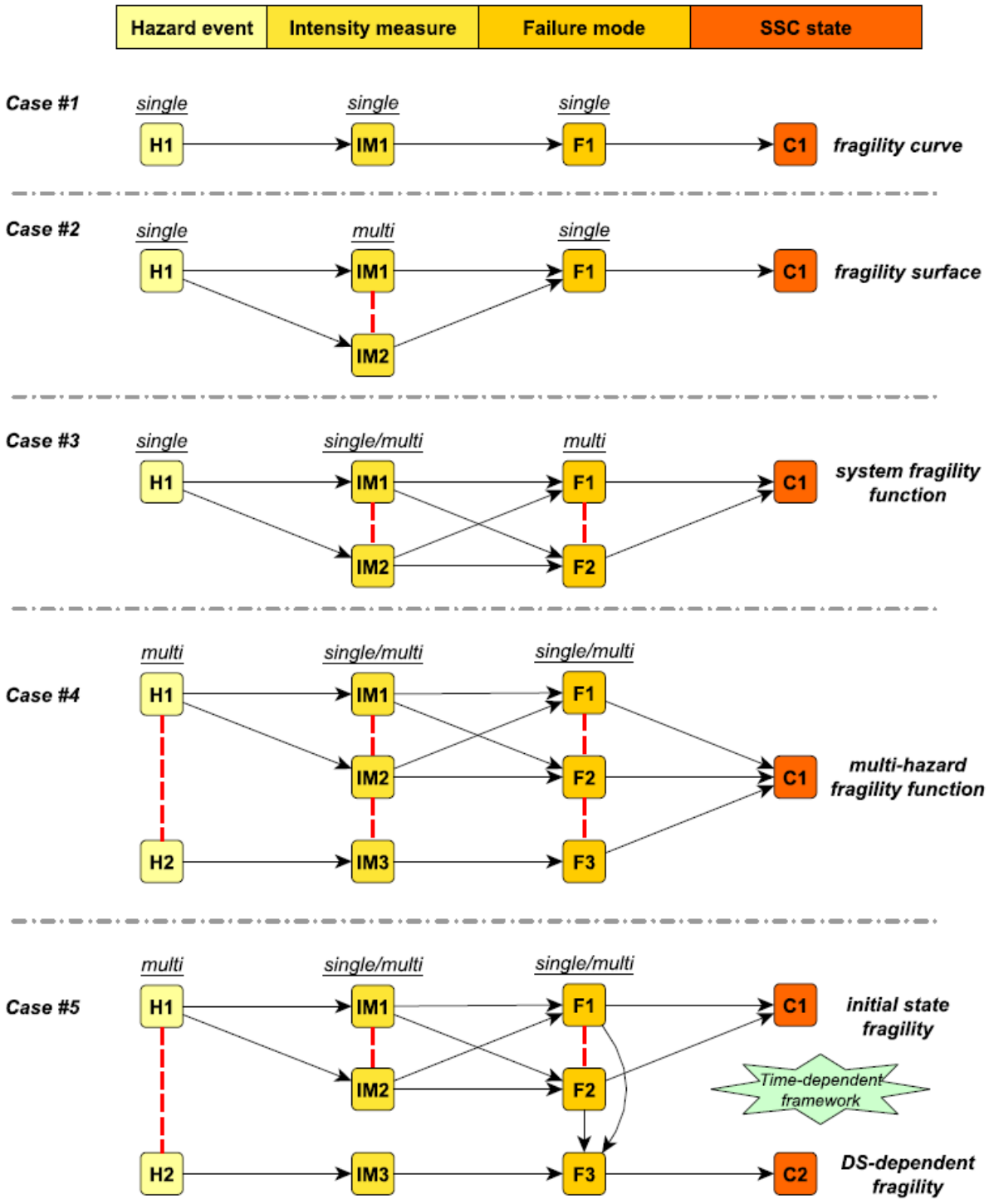

Fig. 20: Decomposition of possible cases to consider within the multi-hazard fragility framework. The black arrows represent dependencies and the red dashed lines represent possible correlations between events.

Case #5 pertains only to sequential hazard events (i.e., occurrence of H1, followed by H2 in a given time window), which may be decomposed into a temporal sequence, where successive loadings are applied at different time scales. In the case where the SSC is subjected to exactly co-occurring physical loadings, then the related IMs are induced by the same source event (e.g., flood hazard generating both inundation due to water depth and lateral loading due to flow velocity; seismic hazard at the origin of both wave propagation and soil deformation effects). Therefore, it may be summarised that case #4 includes hazards with co-occurring loadings (possible representation by joint cumulative distribution functions), while case #5 is devoted to sequential hazards that induce separate loadings (possible representation by DS-dependent fragility functions).

The five cases are further detailed in Table 11, where typical examples of applications are provided for each one of them.

Table 11: Description of the four cases identified for the multi-hazard fragility modelling of SSCs.

Case	Description	Modelling tools	Examples
#1	Standard single-IM case, with a simple IM-EDP relationship.	- Statistical methods in Section 3.3	- Seismic fragility with PGA (Zentner et al., 2017); - Tsunami fragility with water height (De Risi et al., 2016); - Wind fragility with wind speed (Chiodi et al., 2011);
#2	Vector-IM fragility function, usually with a correlation between the IMs.	- Multivariate GLM regression or MLE (e.g., equations used in Sections 4.2 / 4.3)	- Seismic fragility surfaces (Gehl et al., 2013); - Tsunami or flooding fragility surfaces, with water depth and flow velocity as IMs (De Risi et al., 2016);
#3	System fragility function, resulting from the assembly of single component damage events (i.e., combination of failure modes). The correlation between the occurrences of the failure modes, given the IMs, should be taken into account.	- Occurrence of each failure mode: same tools as in cases #1 and #2; - Combination of failure modes into the SSC functionality state: system reliability theory (e.g., Kang et al., 2010), BBNs (e.g., Gehl & Rohmer, 2018);	- Seismic fragility of a bridge system, using component-specific fragility functions related to different bridge components (Li et al., 2014); - Flood fragility of a defense system (dike), with different possible damage mechanisms (Huang et al., 2014);
#4	Multi-hazard fragility functions, where multiple loadings are applied simultaneously to the SSC. Joint pdfs should be considered for the fragility function construction coming from the combination of hazard loadings.	- Multivariate GLM regression or MLE (e.g., equations used in Sections 4.2 / 4.3); - Identification of hazard-specific failure modes and assembly of hazard-harmonized functionality states: same tools as in case #3;	- Multi-hazard fragility function of a bridge system subjected to co-occurring riverine flood and earthquake (Gehl & D'Ayala, 2016); - Multi-hazard fragility function of a building due to water ingress (rain) and wind loading (Pita et al., 2012);
#5	Damage-state-dependent fragility functions where a first hazard loading may degrade the resistance of the SSC or alter the conditions for when a subsequent hazard loading is applied (i.e., sequence of events). The hazards may be correlated (i.e., same source event, or one hazard event triggering another) or independent (i.e., occurrence within the same time window).	- Estimation of the "initial-state" fragility function: same tools as in cases #1, #2, #3 and #4; - In the case of numerical simulations, models that account for the deterioration of materials or components are required in order to update the fragility w.r.t hazard H2, given the damage induced by hazard H1 (i.e., multi-hazard interactions at the level of physical failure modes); - A set of previously damaged SSC models may be generated	- Damage-state-dependent fragility functions for seismic mainshock-aftershock sequences (Song et al., 2016); - Seismic fragility functions of a bridge previously damaged by scour at the foundations (Alipour & Shafei, 2012);

		(i.e; representing the effects of H1), before being subjected to loadings related to H2;	

Within case #5, when independent hazards events are assumed, Selva (2013) has introduced the concept of a persistence time window ΔTp, which is crucial to properly model the effect of a second hazard event while the effects of the first event in terms of vulnerability and exposure are still present. In the context of NPPs, this time window may correspond to the recovery time of damage components or to the mission time, during which some components are designed to function in case of external hazard events: these time windows, as well as the probability of several hazard events occurring during the time interval, will be defined through joint work with the NARSIS work packages in charge of hazard assessment (WP1) and risk integration (WP3). This will allow the implementation of a model implementation that properly captures the interactions between the various events: the assessment of correlated hazards should take into account all the available information (i.e. site-specific, regional, worldwide), as well as the model uncertainties. Finally, at the system level it is important to aggregate the fragility functions of the single components on account of their intercorrelations, that is the fragility curves are being based on the combination of hazards and components.

6 Conclusions

This report has presented a detailed overview of potential fragility derivation methods in the case of SSCs within NPPs. The main emphasis of the report consists in the generation of vector-based fragility functions (i.e., use of vector-IMs as conditioning variables) and the impact of the latter on the identification of the various sources of uncertainties. In the first part of the report, which has been mostly focused on fragility assessment related to seismic hazard, the outcomes of two practical case studies have led to the following observations:

- Carefully selected vector-IMs make excellent candidates in terms of IM sufficiency and efficiency, when compared to scalar IMs.
- Vector-valued fragility functions tend to generate less dispersion (i.e., aleatory uncertainty due to record-to-record variability) than scalar-IM fragility curves: this difference may be interpreted as a partial transfer from the record-to-record variability to an epistemic uncertainty component that is related to the description of the seismic loading given the hazard at the studied site.
- The conditional spectrum method for the selection of input ground-motion records appears to be compatible with the derivation of vector-based fragility functions, since the hazard consistency is maintained throughout the scaling levels: such a framework is especially well adapted when considering spectral accelerations at various periods as vector-IMs.
- Although a wide range of statistical tools are available for the quantification and propagation of sources of uncertainties, it appears that all the epistemic uncertainties usually cannot be adequately covered and accounted for. In most cases, expert judgment would be necessary in order to constrain the assumptions and to interpret the simulation results.

The first phase of Task 2.3 has mostly dwelt on fragility functions for seismic hazard, where multiple intensity measures may be used to accurately represent a given ground-motion time history. What may appear as a specificity of seismic loadings is actually applicable to a wide range of other hazard loadings. This is demonstrated by the rationale that has been developed in Section 5, where multiple intensity measures and physical failure modes can be combined in order to generate fragility models for a wide range of multi-hazard configurations. Provided that the required hazard-specific physical models are available, the statistical tools detailed in the present report are able to cover most of the multi-hazard cases:

- Multivariate GLM regression or MLE are to be used for the estimation of fragility parameters given a set of conditioning variables.
- Algorithms and procedures based on the system reliability theory (e.g., Kang et al., 2010) are able to combine hazard-specific failure modes in order to model the SSC functionality states of a given SSC. Either joint probabilistic of failure or damage-state-dependent fragility functions may be derived from this framework.

The latter point may require the construction of BBNs at the level of the studied SSC (e.g., Gehl & D'Ayala, 2016; Gehl & Rohmer, 2018), which will correspond to the technical sub-networks that are part of the risk integration task (i.e., Work Package 3).

7 References

Abrams, D. (1996). Effects of scale and loading rate with tests of concrete and masonry structures. *Earthquake Spectra*, *12*, 13-28.

Alipour, A., & Shafei, B. (2012). Performance assessment of highway bridges under earthquake and scour effects. In *Proceedings of the 15th world conference on earthquake engineering*, Lisbon, Portugal.

Ang, A.H.S., Tang W.H. (2007). *Probability Concepts in Engineering: Emphasis on Applications to Civil and Environmental Engineering*. John Willey & Sons, NY.

ASAMPSA_E (2013-2016), "Advanced Safety Assessment Methodologies: Extended PSA", FP7 European Project, www.asampsa.eu.

Asprone, D., Jalayer, F., Prota, A., & Manfredi, G. (2010). Proposal of a probabilistic model for multi-hazard risk assessment of structures in seismic zones subjected to blast for the limit state of collapse. *Structural Safety*, *32*(1), 25-34.

ATC (2012). *Seismic Performance Assessment Methodology for Buildings, Volume 1 – Methodology*, Report N°. FEMA P58-1, Federal Emergency Management Agency, Washington, D.C.

Baker, J.W., & Cornell, C.A. (2005). A vector-valued ground motion intensity measure consisting of spectral acceleration and epsilon. *Earthquake Engineering & Structural Dynamics, 34*, 1193-1217.

Baker, J.W., & Jayaram, N. (2008). Correlation of spectral acceleration values from NGA ground motion models. *Earthquake Spectra*, *24*(1), 299-317.

Bazzurro, P., & Cornell, C.A. (1999). Disaggregation of seismic hazard. *Bulletin of the Seismological Society of America*, *89*(2), 501-520.

Bodda, S.S., Sandhu, H.K., & Gupta, A. (2016). Fragility of a Flood Defense Structure Subjected to Multi-Hazard Scenario. In *24th International Conference on Nuclear Engineering* (pp. V004T14A015-V004T14A015), American Society of Mechanical Engineers.

Bojorquez, E., & Iervolino, I. (2011). Spectral shape proxies and nonlinear structural response. *Soil Dynamics and Earthquake Engineering*, *31*(7), 996-1008.

Bonini, M., Rudolph, M.L., & Manga, M. (2016). Long- and short-term triggering and modulation of mud volcano eruptions by earthquakes. *Tectonophysics*, *672*, 190-211.

Boore, D.M., Stewart, J.P., Seyhan, E., & Atkinson, G.M. (2014). NGA-West2 equations for predicting PGA, PGV, and 5% damped PSA for shallow crustal earthquakes. *Earthquake Spectra*, *30*(3), 1057-1085.

Bradley, A.B. (2010). Epistemic Uncertainty in Component Fragility Functions. *Earthquake Spectra*, *26*(1), 41-62.

Bradley, A.B. (2013). A critical examination of seismic response uncertainty analysis in earthquake engineering. *Earthquake Engineering and Structural Dynamics*, *42*(11), 1717-1729

Butler, D.R., Malanson, G.P., & Oelfke, J. (1991). Potential catastrophic flooding from landslide-dammed lakes, Glacier National Park, Montana, USA. *Zeitschrift für Geomorphologie Supplement band*, *83*, 195-209.

Cai, Z., Xie, W.C., Pandey, M.D., & Ni, S.H. (2018a). Determining seismic fragility of structures in nuclear power plants using multiple ground motion parameters – Part I: Methodology. *Nuclear Engineering and Design, 335*, 195-201.

Cai, Z., Xie, W.C., Pandey, M.D., & Ni, S.H. (2018b). Determining seismic fragility of structures in nuclear power plants using multiple ground motion parameters – Part II: Application. *Nuclear Engineering and Design, 335*, 186-194.

Cavalieri, F., Franchin, P., & Giovinazzi, S. (2016). Earthquake-altered flooding hazard induced by damage to storm water systems. *Sustainable and Resilient Infrastructure*, *1*(1-2), 14-31.

Charvet, I., Suppasri, A., Kimura, H., Sugawara, D., & Imamura, F. (2015). Fragility estimations for Kesennuma City following the 2011 Great East Japan Tsunami based on maximum flow depths, velocities and debris impact, with evaluation of the ordinal model's predictive accuracy. *Natural Hazards*, *79*(3), 2073-2099.

Chen, H., Zhang, S., Peng, M., & Zhang, L.M. (2016). A physically- based multi-hazard risk assessment platform for regional rainfall- induced slope failures and debris flows. *Engineering Geology*, *203*, 15-29.

Chinh, D.T., Gain, A.K., Dung, N.V., Haase, D., & Kreibich, H. (2015). Multi-variate analyses of flood loss in Can Tho City, Mekong Delta. *Water*, *8*(1), 6.

Chiodi, R., Asprone, D., Maimone, F., Prota, A., & Ricciardelli, F. (2011). Multi-hazard assessment of steel hangar structures subjected to seismic and wind loads. In *Applied Mechanics and Materials* (Vol. 82, pp. 778-783), Trans Tech Publications.

Cornell, C.A., Jalayer, F., Hamburger, R.O., & Foutch, D.A. (2002). Probabilistic basis for 2000 SAC federal emergency management agency steel moment frame guidelines. *Journal of Structural Engineering*, *128*(4), 526-533.

Crosta, G.B., & Frattini, P. (2003). Distributed modelling of shallow landslides triggered by intense rainfall. *Natural Hazards & Earth System Sciences*, *3*(1/2), 81-93.

Daniell, J.E., Schaefer, A.M., Wenzel, F., Haecker, E., Bruneliere, H., Pellissetti, M., Moussalam, N., Jockenhoevel-Barttfeld, M., Rabour, V., Chaumont, B., Guigeno, Y., Lincot, C., Raimond, E., Prosek, A., Cizelj, L., Volanovski, A., Vardon, P., Mohan, V., Hicks, M., Potempski, S., Kowal, K., Malesa, J., Duval, C., Zentner, I., Dutfoy, A., Le Morvan, T., Wang, Z., & Burgazzi, L. (2018). *Del 1.1 Review of state-of-the art for hazard and multi-hazard characterisation*. WP1 Technical Report, New Approach to Reactor Safety Improvements, www.narsis.eu.

De Pippo, T., Donadio, C., Pennetta, M., Petrosino, C., Terlizzi, F., & Valente, A. (2008). Coastal hazard assessment and mapping in Northern Campania, Italy. *Geomorphology*, *97*(3-4), 451-466.

De Risi, R., & Goda, K. (2016). Probabilistic earthquake–tsunami multi-hazard analysis: application to the Tohoku Region, Japan. *Frontiers in Built Environment*, *2*, 25.

De Risi, R., Goda, K., Yasuda, T., & Mori, N. (2017). Is flow velocity important in tsunami empirical fragility modeling?. *Earth-science reviews*, *166*, 64-82.

Decker, K., & Brinkman, H. (2016). *List of external hazards to be considered in ASAMPSA_E*, Technical Report WP21/D21.2/2017-41, ASAMPSA_E project.

Dietrich, J., et al. (2010). A high-resolution coupled riverine flow, tide, wind, wind wave, and storm surge model for southern Louisiana and Mississippi. II: Synoptic description and analysis of Hurricanes Katrina and Rita. *Mon. Weather Rev.*, *138*(2), 378-404.

Dolsek, M. (2009). Incremental dynamic analysis with consideration of modelling uncertainties. *Earthquake Engineering and Structural Dynamics*, *38*, 805-825.

Douglas, J. (2012). Consistency of ground-motion predictions from the past four decades: peak ground velocity and displacement, Arias intensity and relative significant duration. *Bulletin of Earthquake Engineering*, *10*(5), 1339-1356.

Douglas, J. (2018). "Ground Motion Prediction Equations 1964-2018", www.gmpe.org.uk.

Ellingwood, B. (1990). Validation studies of seismic PRAs. *Nuclear Engineering and Design*, *123*(2-3), 189-196.

EPRI (1994), *Methodology for Developing Seismic Fragilities*, EPRI, Palo Alto, CA: June 1994. TR-103959.

EPRI (2003). *Seismic Probabilistic Risk Assessment Implementation Guide*, EPRI, Palo Alto, CA: December 2003. TR-1002989.

EPRI (2009). *Seismic Fragility Application Guide Update*, EPRI, Palo Alto, CA: December 2009. TR-1019200.

Feuillet, N., Cocco, M., Musumeci, C., & Nostro, C. (2006). Stress interaction between seismic and volcanic activity at Mt Etna. *Geophys. J. Int.*, *164*(3), 697-718.

Franchin, P., & Cavalieri, F. (n.d.). *OOFIMS: Object-Oriented Framework for Infrastructure Modeling and Simulation*, Available at: https://sites.google.com/a/uniroma1.it/oofims.

Garcia-Aristizabal, A., Marzocchi, W., & Di Ruocco. A. (2013). *Probabilistic framework for multi-hazard assessment*, Technical Report D3.4, MATRIX project.

Gehl, P., & D'Ayala, D. (2016). Development of Bayesian Networks for the multi-hazard fragility assessment of bridge systems. *Structural Safety*, *60*, 37-46.

Gehl, P., & Rohmer, J. (2018). Vector intensity measures for a more accurate reliability assessment of NPP sub-systems. In *International Conference on Technological Innovations in Nuclear Civil Engineering*, Paris, France.

Gehl, P., Seyedi, D.M., & Douglas, J. (2013). Vector-valued fragility functions for seismic risk evaluation. *Bulletin of Earthquake Engineering*, *11*(2), 365-384.

Gehl, P., Douglas, J., & Seyedi, D.M. (2015). Influence of the number of dynamic analyses on the accuracy of structural response estimates. *Earthquake Spectra*, *31*(1), 97-113.

Gill, J.C., & Malamud, B.D. (2014). Reviewing and visualizing the interactions of natural hazards. *Reviews of Geophysics*, *52*(4), 680-722.

Goda, K., & De Risi, R. (2018). Multi-hazard loss estimation for shaking and tsunami using stochastic rupture sources. *International journal of disaster risk reduction*, *28*, 539-554.

Hariri-Ardebili, M.A., & Saouma, V.E. (2016). Probabilistic seismic demand model and optimal intensity measure for concrete dams. *Structural Safety*, *59*, 67-85.

Hinkel, J., et al. (2014). Coastal flood damage and adaptation costs under 21st century sea-level rise. *Proc. Natl. Acad. Sci.*, *111*(9), 3292-3297.

Huang, W.C., Weng, M.C., & Chen, R.K. (2014). Levee failure mechanisms during the extreme rainfall event: a case study in Southern Taiwan. *Natural Hazards*, *70*(2), 1287-1307.

Hudson, J. A. (1992). *Rock Engineering System*. Chichester, Ellis Horwood.

Iooss, B., & Lemaître, P. (2015). A review on global sensitivity analysis methods. In *Uncertainty management in simulation-optimization of complex systems*. Springer, Boston, MA.

Jalayer, F., Beck, J.L., & Zareian, F. (2011). Analyzing the sufficiency of alternative scalar and vector intensity measures of ground shaking based on information theory. *Journal of Engineering Mechanics*, *138*(3), 307-316.

Jayaram, N., Lin, T., & Baker, J.W. (2011). A computationally efficient ground-motion selection algorithm for matching a target response spectrum mean and variance. *Earthquake Spectra*, *27*(3), 797-815.

Kafali, C. (2008). *System performance under multi-hazard environment*. PhD Thesis, Cornell University, Ithaca, NY.

Kameshwar, S., & Padgett, J.E. (2014). Multi-hazard risk assessment of highway bridges subjected to earthquake and hurricane hazards. *Engineering Structures*, *78*, 154-166.

Kang, W.H., Lee, Y. J., Song, J., & Gencturk, B. (2012). Further development of matrix-based system reliability method and applications to structural systems. *Structure and Infrastructure Engineering*, *8*(5), 441-457.

Kappes, M.S., Keiler, M., & Glade, T. (2010). Consideration of hazard interactions in medium-scale multi-hazard risk analyses. In *EGU General Assembly Conference Abstracts* (Vol. 12, p. 3331).

Kennedy, R.P., & Ravindra, M.K. (1984). Seismic fragilities for nuclear power plant studies. *Nuclear Engineering and Design, 79*(1), 47-68.

Kennedy, R.P., Cornell, C.A., Campbell, R.D., Kaplan, S., & Perla, H.F. (1980). Probabilistic Seismic Safety Study of an Existing Nuclear Power Plant. *Nuclear Engineering and Design, 59*(2), 305-338.

Kreibich, H., Piroth, K., Seifert, I., Maiwald, H., Kunert, U., Schwarz, J., ... & Thieken, A.H. (2009). Is flow velocity a significant parameter in flood damage modelling?. *Natural Hazards and Earth System Sciences*, *9*, 1679-1692.

Kythe, P.K., & Schaferhotter, M.R., (2000). *Handbook of Computational Methods for Integration*. Chapman and Hall/CRC.

Lee, K.H., & Rosowsky, D.V. (2006). Fragility analysis of woodframe buildings considering combined snow and earthquake loading. *Structural Safety*, *28*(3), 289-303.

Leon, R.T., & Deierlein, G.G. (1996). Considerations for the use of quasistatic testing. *Earthquake Spectra*, *12*, 87-109.

Li, Y., & van de Lindt, J.W. (2012). Loss-based formulation for multiple hazards with application to residential buildings. Engineering Structures, 38, 123–133

Li, Y., van de Lindt, J.W., Dao, T., Bjarnadottir, S., & Ahuja, A. (2011). Loss analysis for combined wind and surge in hurricanes. *Natural hazards review*, *13*(1), 1-10.

Li, Z., Li, Y., & Li, N. (2014). Vector-intensity measure based seismic vulnerability analysis of bridge structures. *Earthquake Engineering and Engineering Vibration, 13*(4), 695-705.

Lin, N., & Vanmarcke, E. (2010a). Windborne debris risk analysis. I: Introduction and methodology. *Wind Struct.*, *13*(2), 191-206.

Lin, N., & Vanmarcke, E. (2010b). Windborne debris risk analysis. II: Application to structural vulnerability modelling. *Wind Struct.*, *13*(2), 207-220.

Lin, T., Haselton, C.B., & Baker, J.W. (2013). Conditional spectrum-based ground motion selection. Part I: hazard consistency for risk-based assessments. *Earthquake engineering & structural dynamics*, *42*(12), 1847-1865.

Liu, B., Siu, Y.L., & Mitchell, G. (2015). Hazard interaction analysis for multi-hazard risk assessment: a systematic classification based on hazard-forming environment. *Natural Hazards and Earth System Sciences*, *18*, 19.

Liu, B., Siu, Y.L., & Mitchell, G. (2017). A quantitative model for estimating risk from multiple interacting natural hazards: an application to northeast Zhejiang, China. *Stochastic Environmental Research and Risk Assessment*, *31*(6), 1319-1340.

Luco, N., & Cornell, C.A. (2007). Structure-specific scalar intensity measures for near-source and ordinary earthquake ground motions. *Earthquake Spectra*, *23*(2), 357-392.

Marzocchi, W., Garcia-Aristizabal, A., Gasparini, P., Mastellone, M.L., & Di Ruocco, A. (2012). Basic principles of multi-risk assessment: a case study in Italy. *Natural hazards*, *62*(2), 551-573.

MATRIX (2010-2013), “New methodologies for multi-hazard and multi-risk assessment”, FP7 European Project, matrix.gpi.kit.edu.

McKay, M.D., Beckman, R.J., & Conover, W.J. (1979). Comparison of three methods for selecting values of input variables in the analysis of output from a computer code. *Technometrics*, *21*(2), 239-245.

Merz, B., Kreibich, H., & Lall, U. (2013). Multi-variate flood damage assessment: a tree-based data-mining approach. *Natural Hazards and Earth System Sciences*, *13*(1), 53-64.

Mignan, A., Wiemer, S., & Giardini, D. (2014). The quantification of low-probability–high-consequences events: part I. A generic multi-risk approach. *Natural Hazards*, *73*(3), 1999-2022.

Modica, A, & Stafford, P.J. (2014). Vector fragility surfaces for reinforced concrete frames in Europe. *Bulletin of Earthquake Engineering, 12*, 1725-1753.

Mudd, L., Rosowsky, D., Letchford, C., & Lombardo, F. (2016). Joint Probabilistic Wind–Rainfall Model for Tropical Cyclone Hazard Characterization. *Journal of Structural Engineering*, *143*(3), 04016195.

Neri, M., Le Cozannet, G., Thierry, P., Bignami, C., & Ruch, J. (2013). A method for multi-hazard mapping in poorly known volcanic areas: an example from Kanlaon (Philippines). *Natural Hazards and Earth System Sciences*.

Nicholls, R.J., Hoozemans, F.M., & Marchand, M. (1999). Increasing flood risk and wetland losses due to global sea-level rise: Regional and global analyses. *Global Environ. Change*, *9*(S1), S69-S87.

Nielsen, E.R., Herman, G.R., Tournay, R.C., Peters, J.M., & Schumacher, R.S. (2015). Double impact: When both tornadoes and flash floods threaten the same place at the same time. *Weather and Forecasting*, *30*(6), 1673-1693.

Padgett, J.E., Nielson, B.G., & DesRoches, R. (2008). Selection of optimal intensity measures in probabilistic seismic demand models of highway bridge portfolios. *Earthquake Engineering & Structural Dynamics*, *37*(5), 711-725.

PEER (2013). *PEER NGA-West2 Database*, Pacific Earthquake Engineering Research Center, https://ngawest2.berkeley.edu.

Phan, L.T., Simiu, E., McInerney, M.A., Taylor, A.A., Glahn, B., & Powell, M.D. (2007). Methodology for development of design criteria for joint hurricane wind speed and storm surge events: proof of concept. *NIST Technical Note 1482*, National Institute of Standards and Technology, Gaithersburg.

Pita, G., Pinelli, J.P., Cocke, S., Gurley, K., Mitrani-Reiser, J., Weekes, J., & Hamid, S. (2012). Assessment of hurricane-induced internal damage to low-rise buildings in the Florida Public Hurricane Loss Model. *Journal of Wind Engineering and Industrial Aerodynamics*, *104*, 76-87.

Prasad, G., & Banerjee, S. (2013). The impact of flood-induced scour on seismic fragility characteristics of bridges. *Journal of Earthquake Engineering*, *17*(6), 803-828.

Rahni, N., Lancieri, M., Clement, C., Nahas, G., Clement, J., Vivan, L., Guigueno, Y., & Raimond, E. (2017). An original approach to derived seismic fragility curves – Application to a PWR main steam line. In *Proceedings of the International Topical Meeting on Probabilistic Safety Assessment and Analysis (PSA2017)*, Pittsburgh, PA.

Ribeiro, F.L., Barbosa, A.R., & Neves, L.C. (2014). Application of reliability-based robustness assessment of steel moment resisting frame structures under post-mainshock cascading events. *Journal of Structural Engineering*, *140*(8), A4014008.

Rigby, R.A., & Stasinopoulos, D.M. (2005). Generalized additive models for location, scale and shape. *Journal of the Royal Statistical Society: Series C (Applied Statistics)*, *54*(3), 507-554.

Roueche, D.B. (2018). Epistemic Uncertainties in Fragility Functions Derived from Post-Disaster Damage Assessments. *ASCE-ASME Journal of Risk and Uncertainty in Engineering Systems, Part A: Civil Engineering*, *4*(2), 04018015.

Rossetto, T., Gehl, P., Minas, S., Galasso, C., Duffour, P., Douglas, J., & Cook, O. (2016). FRACAS: A capacity spectrum approach for seismic fragility assessment including record-to-record variability. *Engineering Structures*, *125*, 337-348.

Sadegh, M., Moftakhari, H., Gupta, H.V., Ragno, E., Mazdiyasni, O., Sanders, B., Matthew, R., & AghaKouchak, A. (2018). Multihazard scenarios for analysis of compound extreme events. *Geophysical Research Letters*, *45*(11), 5470-80.

Sainct, R., Feau, C., Martinez, J.M., & Garnier J. Efficient Seismic fragility curve estimation by Active Learning on Support Vector Machines. *Submitted*.

Saltelli, A., Ratto, M., Andres, T., Campolongo, F., Cariboni, J., Gatelli, D., ... & Tarantola, S. (2008). *Global sensitivity analysis: the primer*. John Wiley & Sons.

Selva, J. (2013). Long-term multi-risk assessment: statistical treatment of interaction among risks. *Natural hazards*, *67*(2), 701-722.

Seyedi, D.M., Gehl, P., Douglas, J., Davenne, L., Mezher, N., & Ghavamian, S. (2010). Development of seismic fragility surfaces for reinforced concrete buildings by means of nonlinear time-history analysis. *Earthquake Engineering & Structural Dynamics*, *39*(1), 91-108.

Shinozuka, M., Feng, M., Lee, J., & Naganuma, T. (2000). Statistical analysis of fragility curves. *Journal of Engineering Mechanics*, *126*(12), 1224-1231.

Shome, N., & Williams, C. (2014). Aftershock risk in Japan following Tohoku earthquake. In *10th U.S. National Conference on Earthquake Engineering*, Anchorage, Alaska.

Simeoni, U., Calderoni, G., Tessari, U. & Mazzini, E. (1999). A new application of system theory to foredunes intervention strategies. *Journal of Coastal Research*, *15*(2), 457-470.

Song, R., Li, Y., & van de Lindt, J.W. (2016). Loss estimation of steel buildings to earthquake mainshock–aftershock sequences. *Structural Safety*, *61*, 1-11.

Stewart, J.P., et al. (2015). Selection of ground motion prediction equations for the global earthquake model. *Earthquake Spectra*, *31*(1), 19-45.

Straub, D., & Der Kiureghian, A. (2008). Improved seismic fragility modelling from empirical data. *Structural Safety*, *30*, 320-336.

Sudret, B., Mai, C., & Konakli, K. (2014). Assessment of the lognormality assumption of seismic fragility curves using non-parametric representations. *arXiv preprint arXiv:1403.5481*.

Tyagunov, S., Vorogushyn, S., Muñoz Jimenez, C., Parolai, S., & Fleming, K. (2018). Multi-hazard fragility analysis for fluvial dikes in earthquake-and flood-prone areas. *Natural Hazards and Earth System Sciences*, *18*(9), 2345-2354.

Vamvatsikos, D., & Cornell, C.A. (2002). Incremental dynamic analysis. *Earthquake Engineering & Structural Dynamics*, *31*(3), 491-514.

Venanzi, I., Lavan, O., Ierimonti, L., & Fabrizi, S. (2018). Multi-hazard loss analysis of tall buildings under wind and seismic loads. *Structure and Infrastructure Engineering*, 1-17.

Wang, Z., Zentner, I., & Zio, E. (2018). A Bayesian framework for estimating fragility curves based on seismic damage data and numerical simulations by adaptive neural networks. *Nuclear Engineering and Design*, *338*, 232-246.

Wasserman, L. (2004). *All of statistics: A Concise Course on Statistical Inference*. Springer, NY.

Wen, W., Zhai, C., Ji, D., Li, S. & Xie, L. (2017). Framework for the vulnerability assessment of structure under mainshock-aftershock sequences. *Soil Dynamics and Earthquake Engineering*, *101*, 41-52.

Woessner, J., Danciu, L., Kaestli, P., & Monelli, D. (2013). *Database of seismogenic zones, Mmax, earthquake activity rates, ground motion attenuation relations and associated logic trees.* FP7 SHARE Deliverable Report D6.6.

Wood, S.N., Pya, N., & Säfken, B. (2016). Smoothing parameter and model selection for general smooth models. *Journal of the American Statistical Association*, *111*(516), 1548-1563.

Yilmaz, T. (2015). *Risk assessment of highway bridges under multi-hazard effect of flood-induced scour and earthquake*, PhD thesis, Pennsylvania State University, State College, PA.

Zentner, I. (2010). Numerical computation of fragility curves for NPP equipment. *Nuclear Engineering and Design*, *240*(6), 1614-1621.

Zentner, I., Gündel, M., & Bonfils, N. (2017). Fragility analysis methods: Review of existing approaches and application. *Nuclear Engineering and Design*, *323*, 245-258.

Zuccaro, G., Cacace, F., Spence, R.J.S., & Baxter, P.J. (2008). Impact of explosive eruption scenarios at Vesuvius. *Journal of Volcanology and Geothermal Research*, *178*(3), 416-453.

8 Appendix A: Definition of seismic ground-motion parameters

IM abbrevation	Definition
PGA	Peak Ground Acceleration
PGV	Peak Ground Velocity
PGD	Peak Ground Displacement
AI	Arias Intensity
SA(T)	Spectral Acceleration at period T
A95	Level of acceleration that contains 95% of the Arias intensity
SL75 (95)	Slope of the Husid plot (cumulative AI over time) between 5% and 75% (and 95%) of the total AI
ARMS	Root-Mean-Square Acceleration: square-root of the integral of squared acceleration over time
ASI	Acceleration Spectral Intensity: integral of SA between two periods (here, 0.1s and 0.5s)
DCy	Cyclic Damage parameter: sum of the squared amplitude of all half-cycles, with the rainflow counting method
NCy	Number of effective Cycles: the same as DCy, except that the half-cycles' amplitudes are normalized by the amplitude of the largest half-cycles in the signal
RSD75 (95)	Relative Significant Duration: length of time interval between when AI first exceeds 5% of total value and when AI first exceeds 75% (and 95%) of total value
SI	Housner Spectral Intensity
NED	Normalised Energy Density: integral over time of the squared ground velocity
JMA	Japanese Meteorological Agency instrumental intensity
SMA (SMV)	Sustained Maximum Acceleration (and Velocity): the third highest value of the absolute maximum acceleration (and velocity)
CAV	Cumulative Absolute Velocity: integral over time of the absolute acceleration time-history